

Chromium breathing pyrochlores as a showcase for a variety of pyrochlore Hamiltonians

Pratyay Ghosh,¹ Yasir Iqbal,¹ Tobias Müller,² Ronny Thomale,²
Johannes Reuther,³ Michel J. P. Gingras,^{4,5} and Harald O. Jeschke⁶

¹*Department of Physics, Indian Institute of Technology Madras, Chennai 600036, India*

²*Institute for Theoretical Physics and Astrophysics,*

Julius-Maximilians-Universität Würzburg, Am Hubland, 97074 Würzburg, Germany

³*Dahlem Center for Complex Quantum Systems and Fachbereich Physik,
Freie Universität Berlin, 14195 Berlin, Germany*

⁴*Department of Physics and Astronomy, University of Waterloo, Waterloo, Ontario, N2L 3G1, Canada*

⁵*Quantum Materials Program, Canadian Institute for Advanced Research, MaRS Centre,
West Tower 661 University Ave., Suite 505, Toronto, ON, M5G 1M1, Canada*

⁶*Research Institute for Interdisciplinary Science, Okayama University, Okayama 700-8530, Japan*

(Dated: March 6, 2019)

We investigate all six structurally characterized chromium-based breathing pyrochlores using a combination of density functional theory and pseudofermion functional renormalization group calculations. We show that the distinct magnetic behavior of the materials $\text{LiInCr}_4\text{O}_8$, $\text{LiGaCr}_4\text{O}_8$, $\text{LiInCr}_4\text{S}_8$, $\text{LiGaCr}_4\text{S}_8$, $\text{CuInCr}_4\text{S}_8$ and $\text{CuInCr}_4\text{Se}_8$ can be matched one-to-one to their chemical composition, namely, oxides, sulfides and the selenide, with each realizing very different pyrochlore Hamiltonians. While the oxides form breathing pyrochlore antiferromagnets displaying correlations reminiscent of a perturbed Coulomb spin ice phase, in the sulfides, the ground state degeneracy exhibits a dimensional reduction leading to line-like degeneracies in momentum space originating from an effective face centered cubic lattice mapping in the low temperature regime. In the selenide we reveal the presence of an approximate spiral spin liquid characterized by a sphere-like degenerate manifold of states in reciprocal space. This rich variety of effects is rooted in the subtle interplay of longer-range exchange couplings, upto third nearest-neighbor on the pyrochlore lattice, and also holds the key to successfully describing the available experimentally observed magnetic response of the sulfides and the selenide. We suggest further experimental explorations of chromium breathing pyrochlores as a versatile material platform for investigating the many faces of magnetic frustration.

I. INTRODUCTION

Pyrochlore lattices exhibit intriguing phenomena by virtue of magnetic frustration originating from antiferromagnetic interactions on the corner-sharing tetrahedral network which lead to a massive classical ground state degeneracy [1]. Breathing pyrochlores are characterized by the alternation of small and large tetrahedra, adding a degree of freedom and complexity and richness to the pyrochlore Hamiltonian [2, 3]. Over half-a-century ago, an ordered arrangement of two cations A and A' on the A site of chromium oxospinel $\text{LiInCr}_4\text{O}_8$ and $\text{LiGaCr}_4\text{O}_8$ was first reported [4]. The ordered occupation of the tetrahedral A sites by small and large ions lowers the symmetry of the spinel AB_2X_4 structure from $Fd\bar{3}m$ (no. 227 space group) to $F\bar{4}3m$ (no. 216 space group) [5] and introduces two different nearest-neighbor exchange paths of the magnetic ions on the B site. Ordered 1:1 occupation of the A site were observed in chromium spinels for A cations from (Li, Ga, In, Cu, Ag) and for X anions ($X = \text{O}, \text{S}, \text{Se}$) [5–7]. While chromium spinels in general [8] and breathing chromium spinels in particular [9–15] had been the subject of many experimental investigations over the years, the work of Okamoto *et al.* [16] brought the breathing degree of freedom in the pyrochlore lattice into sharp focus instilling interests in these systems.

On the experimental front, careful analysis of the temperature dependence of the nuclear spin-lattice relaxation rate using ^7Li nuclear magnetic resonance indicated a complex sequence of structural and magnetic phase transitions in $\text{LiInCr}_4\text{O}_8$ and $\text{LiGaCr}_4\text{O}_8$ [17]. X-ray scattering and muon spin rotation revealed more details [18, 19]. Dielectric measurements found anomalies in the vicinity of the antiferromagnetic ordering temperatures of $\text{LiInCr}_4\text{O}_8$ and $\text{LiGaCr}_4\text{O}_8$ [20]. The presence of strong spin-lattice coupling was inferred based on the observation of a half magnetization plateau from high magnetic field measurements on $\text{LiInCr}_4\text{O}_8$ [21]. More recently, several studies have been devoted to the mixed systems $\text{LiGa}_{1-x}\text{In}_x\text{Cr}_4\text{O}_8$ where, upon doping, a rapid suppression of the complex magnetic and structural transitions is observed [22–24].

Theoretically, the properties of the classical breathing pyrochlore Hamiltonian have been carefully investigated [2]. Spin correlations in the ground state [25] and the effects of spin-lattice coupling [26, 27] have been explained. Possible implications of the topological properties of the breathing pyrochlore lattice have been pointed out [28, 29]. One also noteworthy breathing pyrochlore material, $\text{Ba}_3\text{Yb}_2\text{Zn}_5\text{O}_{11}$ with pseudospin $S = 1/2$ Yb^{3+} ions has also been the subject of recent attention [30–32].

Here, we focus on the semiclassical $S = 3/2$ Cr^{3+} breathing pyrochlores which offer, due to the great va-

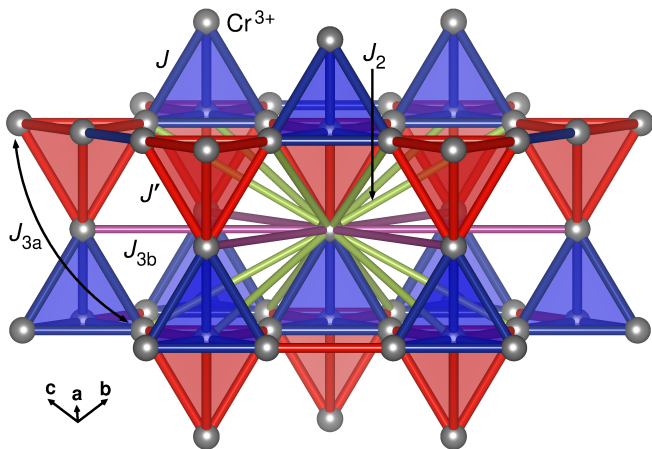


FIG. 1. (Color online) Section of the breathing pyrochlore structure, highlighting first, second and third nearest neighbors for the central Cr^{3+} ion. We use J , J' to label the two nearest-neighbor exchange paths within small (blue) and large (red) tetrahedra, respectively. Note that J_2 connects Cr^{3+} ions of small and large tetrahedra so that there is only one kind. J_{3a} and J_{3b} are the two symmetry inequivalent third nearest neighbors; the J_{3a} features a Cr^{3+} ion in-between, and the J_{3b} does not.

riety of A site cations and X site anions, a diversely rich family of breathing pyrochlore Hamiltonians. Besides the oxides $\text{LiInCr}_4\text{O}_8$ and $\text{LiGaCr}_4\text{O}_8$ [16, 18], the sulfides $\text{LiInCr}_4\text{S}_8$, $\text{LiGaCr}_4\text{S}_8$ and $\text{CuInCr}_4\text{S}_8$ [33, 34], and the selenide $\text{CuInCr}_4\text{Se}_8$ [15] have been fully characterized structurally and are thus amenable to reliable microscopic theoretical modeling. Note that due to the added complication of two magnetic species, we do not consider $\text{CuFeCr}_4\text{S}_8$ [35] or $\text{LiFeCr}_4\text{O}_8$ [36] here before having first fleshed out the properties of the simpler systems with a single magnetic ion. Besides room temperature structures, a low temperature structure has been determined for $\text{LiInCr}_4\text{O}_8$ [18] and $\text{LiGaCr}_4\text{S}_8$ [33], allowing us to partially study the question of the temperature dependence of magnetic Hamiltonians.

In this work, we address the situation that, in spite of the wealth of experimental findings for chromium breathing pyrochlores, knowledge about their underlying Hamiltonians is essentially limited to a few experimental estimates of the breathing anisotropy of the Heisenberg exchange couplings (J for short and J' for long bonds, respectively [see Figure 1]), defining the breathing factor $B_f \equiv J'/J$ [16]. We apply energy mapping techniques within density functional theory to extract the Heisenberg Hamiltonian parameters for the majority of A site ordered chromium breathing pyrochlores with known structures. We find that the behavior of the two oxides is similar, but differs markedly from that of the three sulfides, while the three sulfides display rather similar behavior. Finally, the magnetic ground state of the selenide compound is very different compared to the oxides and sulfides. Thus, the magnetic behavior of the

materials turns out to fall into three groups: that of oxides, sulfides, and the selenide. While $\text{LiInCr}_4\text{O}_8$ and $\text{LiGaCr}_4\text{O}_8$ feature antiferromagnetic J and J' interactions, $\text{LiInCr}_4\text{S}_8$, $\text{LiGaCr}_4\text{S}_8$ and $\text{CuInCr}_4\text{S}_8$ have J and J' of opposite sign, and for $\text{CuInCr}_4\text{Se}_8$ J and J' turn out to be both ferromagnetic. Beyond this, a completely new and thus hitherto unappreciated aspect of the Hamiltonians we find is the presence of sizable longer range couplings with large coordination numbers, and which are expected from studies of the J_1 - J_2 Heisenberg model on the pyrochlore lattice to dramatically alter the displayed behavior of the material [3]. Subsequently, we employ both the classical iterative energy minimization scheme and the quantum approach of pseudofermion functional renormalization group (PFFRG) to calculate the magnetic susceptibilities and ordering temperatures for the full set of exchange couplings entering the model Hamiltonians as determined from DFT. Furthermore, from the PFFRG analysis, we are able to distill and demonstrate the crucial role of the (subleading) longer-range couplings beyond J and J' in accurately capturing and understanding the observed experimental behavior of the materials.

II. METHODS

A. Energy mapping method

We determine the electronic structure and total energies of the breathing pyrochlores with the full potential local orbital (FPLO) basis set [37] and the generalized gradient approximation (GGA) functional [38]. The GGA+ U [39] correction to the exchange and correlation functional is used to deal with the strong electronic correlations on the Cr^{3+} $3d$ orbitals. Of the two parameters entering these calculations, the Hund's rule coupling for Cr^{3+} $3d$ was fixed at $J_H = 0.72$ eV [40]. Meanwhile, the on-site interaction U is determined from the experimentally determined Curie-Weiss temperatures as explained below. Heisenberg Hamiltonian parameters are extracted by energy mapping [41–44]: For this purpose, a $3 \times 1 \times 1$ supercell of the primitive unit of the cubic $F43m$ structure with Cm space group is constructed. In this structure, there are 9 independent spins (out of 12 in total), allowing 75 spin configurations with different energies. Total energies are converged using $6 \times 6 \times 6$ k points. An arbitrary subset of 19 spin configurations allows us to fit six exchange interactions, using a Heisenberg Hamiltonian of the form

$$H = \sum_{i < j} J_{ij} \mathbf{S}_i \cdot \mathbf{S}_j. \quad (1)$$

Note that we count every bond only once. The quality of the fit is seen to be excellent [see Figure 11 in Appendix A for an example], indicating that the method works extremely well for the chromium breathing pyrochlores, be they dominantly antiferromagnetic or ferromagnetic. Now, the U parameter of the GGA+ U func-

tional can be fixed: We calculate the Hamiltonian parameters for a small set of U values which we choose such that the Curie-Weiss temperatures $\Theta_{\text{CW}} = -\frac{1}{3}S(S+1)(3J+3J'+12J_2+6J_{3a}+6J_{3b})$ [see Figure 1] obtained classically from these Hamiltonians cover a range of temperatures which includes the experimental Θ_{CW} ; we find the U value from the condition $\Theta_{\text{CW}}^{\text{theor}} = \Theta_{\text{CW}}^{\text{exp}}$ by interpolation [see Figure 2]. For the breathing pyrochlores, we find the $\Theta_{\text{CW}}^{\text{theor}}$ to be monotonous functions of U and thus to allow for a unique solution [45].

B. Pseudofermion functional renormalization group method

In the PFFRG scheme [46–49], a general spin- S Heisenberg Hamiltonian, e.g. Eq. (1) is treated by first re-expressing the spin operator at each lattice site by $2S$ spin-1/2 degrees of freedom using Abrikosov pseudofermions. Aside from the desired Hilbert space of spin- S states this, however, also introduces unphysical states with lower spin magnitudes. Since these states contribute less to the energy of the system compared to the physical ones, they act as excitations and, thus, naturally get excluded at low temperatures in the RG process [3]. Next, the pseudo-fermionic Hamiltonian is treated using the Functional Renormalization Group (FRG) formalism. Here, the bare fermionic Green's function in Matsubara space is equipped with an infrared frequency cut-off Λ suppressing the fermionic propagation at low frequencies. The PFFRG flow equations then follow from the Λ dependence of the m -particle irreducible vertex functions which are given by an exact and infinite hierarchy of coupled integro-differential flow equations [50, 51]. For a numerical implementation, this hierarchy however needs to be truncated, which is done by neglecting three-particle and higher vertex functions. Most importantly, the truncated version of the method still exactly sums up the full set of fermionic Feynman diagrams in two limits taken separately, namely, the large- S limit [52] and the large- N limit [53]. In doing so, it provides an unbiased analysis of the competition between magnetic ordering and disordering tendencies [3, 46, 50–52].

The flow equations are numerically solved in direct space and after the Fourier transform of the spin-spin correlations, the physical outcome is the static susceptibility in reciprocal space $S(\mathbf{q})$ as a function of Λ . Note that the RG parameter Λ can be interpreted as the temperature T [3] and will therefore be used to investigate the thermal evolution of the magnetic response. In the present study, we evaluate spin correlators inside a cube of edge length of $5a$ where a is the cubic lattice constant, which incorporates a total of 2315 correlated sites, producing well converged results with a high \mathbf{q} -space resolution. Furthermore, we approximate the frequency dependence of the vertex functions by discrete grids containing 64 points for each frequency variable. An ordered system is identified by cusps or kinks in the susceptibility

flow signaling a magnetic instability [46]. In contrast, a smooth flow of the susceptibility down to $\Lambda \rightarrow 0$ indicates a magnetically disordered state, that is a putative (quantum) spin liquid.

C. Iterative minimization method

Employing the iterative minimization method [3, 54], we find the ground state of the classical version of Eq. (1) obtained by replacing the spin operators by normalized vectors. In this scheme, we typically start from a random spin configuration, randomly select one vector-spin \mathbf{S}_i at a time and rotate it to make it antiparallel to its local field

$$\mathbf{h}_i = \frac{\delta H}{\delta \mathbf{S}_i}, \quad (2)$$

thus minimizing the energy. In a given sweep we update as many spins as are contained in the configuration so that on average each spin is updated once. For our calculations we use 32 cubic unit cells of the pyrochlore lattice in each direction with periodic boundary conditions, totaling to $16 \times 32^3 = 524288$ spins in the system. Convergence is reached once the total energy difference per sweep is less than 10^{-10} K. To reduce the likelihood of getting stuck at a local energy minimum in configuration space, we do the minimization for at least 20 different random initial configurations. We also use arbitrary non-random configurations, e.g. spin spirals, as a starting point, to test exact spin parameterizations and, possibly, find lower minimal energies.

III. RESULTS

A. Breathing pyrochlore Hamiltonians

1. Room temperature structures

First, we perform electronic structure calculations for all available room temperature structures of chromium breathing pyrochlores. We use the structures of Okamoto *et al.* (Ref. [16]) for $\text{LiInCr}_4\text{O}_8$ and $\text{LiGaCr}_4\text{O}_8$, the structures of Okamoto *et al.* (Ref. [34]) for $\text{LiInCr}_4\text{S}_8$, $\text{LiGaCr}_4\text{S}_8$ and $\text{CuInCr}_4\text{S}_8$ and that of Duda *et al.* (Ref. [15]) for $\text{CuInCr}_4\text{Se}_8$. The main exchange paths of all structures are illustrated in Figure 1. We follow the experimental literature [16–19] in referring to the exchange couplings in the small and large tetrahedra as J and J' , respectively. As in the isotropic pyrochlore lattice [55], there are twelve second nearest neighbors J_2 and twelve third nearest neighbors which split into two symmetry inequivalent classes; six of these, named J_{3a} , do have an intermediate Cr^{3+} ion, and the six others, named J_{3b} , do not.

Figure 2 presents the first main result of our work. The exchange couplings as defined in Eq. (1) are shown

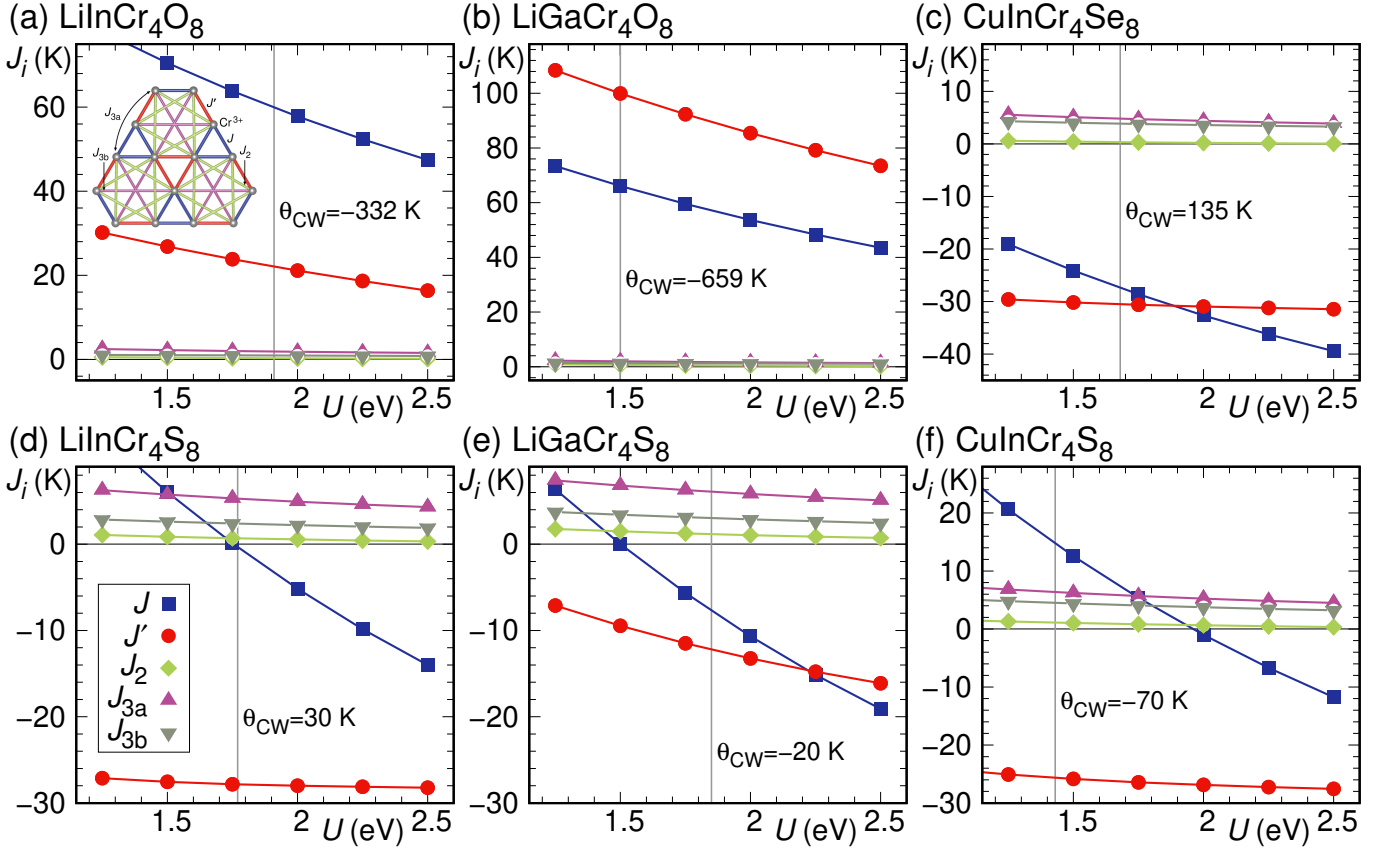


FIG. 2. (Color online) Exchange couplings of six breathing pyrochlore compounds as function of interaction strength U . The vertical lines indicate the U value at which the known experimental Curie-Weiss temperature is reproduced. The inset of (a) shows a single kagome plane cut out of the pyrochlore lattice to visualize the exchange paths.

TABLE I. Exchange couplings of six chromium breathing pyrochlore compounds, calculated within GGA+ U at $J_H = 0.72$ eV. The values of the J_i are given with respect to classical spins of length $S = 3/2$ and without double counting of bonds [see Eq. (1)].

| Material | U (eV) | J (K) | J' (K) | J_2 (K) | J_{3a} (K) | J_{3b} (K) | Θ_{CW} (K) |
|-------------------------------------|----------|----------|----------|-----------|--------------|--------------|-------------------|
| LiInCr ₄ O ₈ | 1.91 | 59.8(2) | 22.0(2) | 0.3(1) | 1.9(1) | 0.9(1) | -332 |
| LiGaCr ₄ O ₈ | 1.50 | 66.2(3) | 100.0(2) | 0.7(1) | 2.0(1) | 1.3(1) | -658 |
| LiInCr ₄ S ₈ | 1.77 | -0.3(1) | -28.0(1) | 0.7(1) | 5.3(1) | 2.4(1) | 30 |
| LiGaCr ₄ S ₈ | 1.85 | -7.7(1) | -12.2(1) | 1.2(1) | 6.1(1) | 3.0(1) | -20 |
| CuInCr ₄ S ₈ | 1.43 | 14.7(1) | -26.0(1) | 1.1(1) | 6.4(1) | 4.5(1) | -70 |
| CuInCr ₄ Se ₈ | 1.68 | -25.4(2) | -31.0(1) | 0.3(1) | 4.8(1) | 3.9(1) | 135 |

as a function of U in the GGA+ U functional. For all six compounds, a U value can be determined at which the couplings yield the experimental Curie-Weiss temperature (vertical lines). These fixed parameter values lead to the sets of Hamiltonian couplings shown in Table I. The U values are very reasonable for Cr³⁺ and are all located in a narrow interval $1.43 \text{ eV} \leq U \leq 1.91 \text{ eV}$, indicating that the great diversity among the chromium breathing pyrochlores varying from antiferromagnetic to ferromagnetic Heisenberg models can all be described with roughly the same exchange correlation functional. We find that both oxides, LiInCr₄O₈ and LiGaCr₄O₈, are dominated by antiferromagnetic J and J' couplings (Fig-

ure 2 (a) and (b)); longer range couplings are negligibly small. Contrary to the naive expectation, for LiGaCr₄O₈ the large tetrahedron is associated with the larger exchange coupling. The calculated breathing anisotropy for LiGaCr₄O₈ is $B_f = J/J' = 0.66$, very close to the experimental estimate $B_f = 0.6$ [16]. However, according to our calculation, LiInCr₄O₈ at $B_f = J'/J = 0.37$ is far less anisotropic than estimated experimentally ($B_f = 0.1$) [16]. For the sulfides LiInCr₄S₈, LiGaCr₄S₈ and CuInCr₄S₈ (Figure 2 (c)-(e)), the large tetrahedra become ferromagnetic. The big surprise is the presence of substantial second- and third-neighbor couplings. As each Cr³⁺ ion has a total of 24 such bonds, compared to

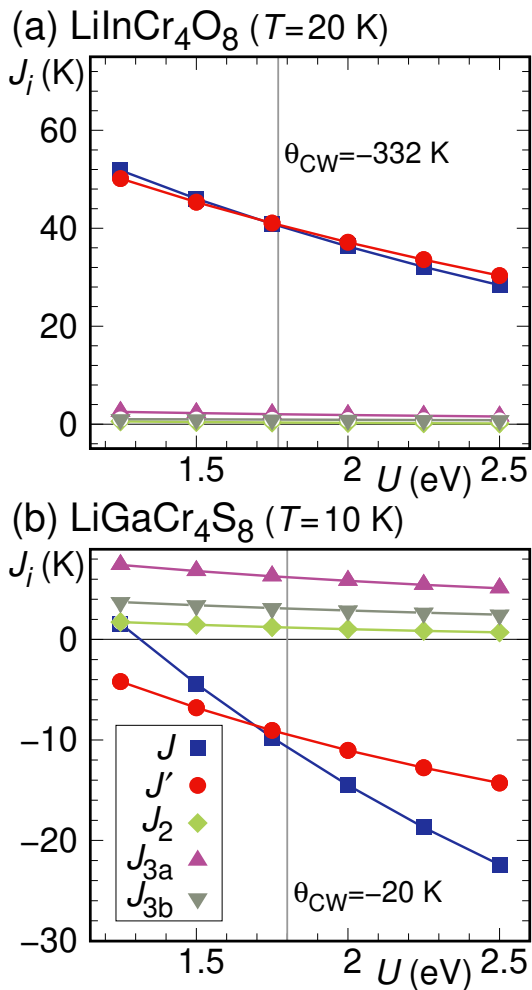


FIG. 3. (Color online) Exchange couplings for two low temperature structures [18, 33] of breathing pyrochlore compounds as function of interaction strength U . Vertical lines indicate the U value at which the experimental Curie-Weiss temperature is realized.

six J or J' bonds, they can have a substantial influence on the behavior of the materials. Interestingly, the fact that

| Material | T (K) | $r \equiv d_{\text{Cr-Cr}}^J$ (Å) | $r' \equiv d_{\text{Cr-Cr}}^{J'}$ (Å) | r'/r |
|--|------------|--------------------------------------|--|--------|
| LiInCr ₄ O ₈ [18] | 20 | 2.929 | 3.014 | 1.029 |
| LiInCr ₄ O ₈ [16] | RT | 2.903 | 3.051 | 1.051 |
| LiGaCr ₄ O ₈ [16] | RT | 2.867 | 2.970 | 1.036 |
| LiInCr ₄ S ₈ [34] | RT | 3.429 | 3.735 | 1.089 |
| LiGaCr ₄ S ₈ [33] | 10 | 3.404 | 3.641 | 1.070 |
| LiGaCr ₄ S ₈ [34] | RT | 3.397 | 3.649 | 1.074 |
| CuInCr ₄ S ₈ [34] | RT | 3.405 | 3.709 | 1.089 |
| CuInCr ₄ Se ₈ [15] | RT | 3.613 | 3.864 | 1.070 |

TABLE II. Two smallest $\text{Cr}^{3+}-\text{Cr}^{3+}$ distances r and r' for the investigated breathing pyrochlores, together with the (lattice) breathing anisotropy r'/r . RT stands for room temperature.

the experimentally determined Curie-Weiss temperature of LiGaCr₄S₈ is small is thus explained by a cancellation of ferromagnetic J and J' by antiferromagnetic J_2 and J_{3a} , J_{3b} couplings rather than by opposite signs of J and J' as hypothesized in Ref. [34]. Opposite signs of J and J' are only found for CuInCr₄S₈. Finally, the selenide CuInCr₄Se₈ (Figure 2 (c)) is most clearly dominated by ferromagnetic J and J' couplings; however, even for this compound, the third neighbor couplings J_{3a} and J_{3b} are antiferromagnetic and, most importantly, non-negligible.

2. Temperature dependence

For most materials, only a room temperature structure is on record. However, in Ref. [18], lattice parameters for a $T = 20$ K LiInCr₄O₈ structure are given [56]. Furthermore, Pokharel *et al.* [33] provide a $T = 10$ K structure of LiGaCr₄S₈. The two Cr-Cr distances within small and large tetrahedra for these two structures are tabulated along with the measurements of the six room temperature structures in Table II. While the breathing anisotropy of the oxide LiInCr₄O₈ decreases significantly at low temperature, it is essentially temperature independent for the sulfide LiGaCr₄S₈. Studying the two cubic low temperature structures can give us an indication of how temperature dependent the electronic behavior of the breathing pyrochlore materials is within the cubic $F\bar{4}3m$ structure. Clearly, a systematic study of the temperature dependence of the exchange couplings would require more detailed structural information for the other materials. Table III shows the exchange interactions calculated for the two low temperature structures. Even though the low temperature structure of LiInCr₄O₈ has a breathing anisotropy of $r'/r = 1.029$, the exchange couplings J and J' become nearly identical [see Figure 3], with the room temperature exchange anisotropy of $J'/J = 0.37$ having been eliminated. For LiGaCr₄S₈, while the low temperature structural anisotropy is still large at $r'/r = 1.070$, the two ferromagnetic couplings J and J' become very similar near the U value determined by the experimental Θ_{CW} [see Figure 3]. Thus, we find that the nearest-neighbor exchanges J and J' remain antiferromagnetic for LiInCr₄O₈ and ferromagnetic for LiGaCr₄S₈, but become very similar at low temperatures; the further neighbor couplings remain very small for the oxide and substantial for the sulfide.

Energy mapping clearly identifies three different types of breathing pyrochlore Hamiltonians: Mostly antiferromagnetic oxides, sulfides with ferromagnetic large tetrahedron and antiferromagnetic longer range exchange, and the mostly ferromagnetic selenide perturbed by crucial antiferromagnetic longer range interactions. Thus, we organize our pseudofermion functional renormalization group analysis of the Hamiltonians into oxide, sulfide and selenide sections.

TABLE III. Exchange couplings corresponding to the low temperature structures of $\text{LiInCr}_4\text{O}_8$ ($T = 20$ K [18]) and $\text{LiGaCr}_4\text{S}_8$ ($T = 10$ K [33]) calculated using GGA+ U at $J_{\text{H}} = 0.72$ eV. The values of the J_i are given with respect to spin operators of length $S = 3/2$ and without double counting of bonds [see Eq. (1)].

| Material | U (eV) | J (K) | J' (K) | J_2 (K) | J_{3a} (K) | J_{3b} (K) | Θ_{CW} (K) |
|-----------------------------|----------|----------|----------|-----------|--------------|--------------|--------------------------|
| $\text{LiInCr}_4\text{O}_8$ | 1.77 | 40.6(2) | 40.8(2) | 0.3(1) | 2.0(1) | 0.9(1) | -332 |
| $\text{LiGaCr}_4\text{S}_8$ | 1.80 | -10.8(1) | -9.5(1) | 1.2(1) | 6.2(1) | 3.1(1) | 30 |

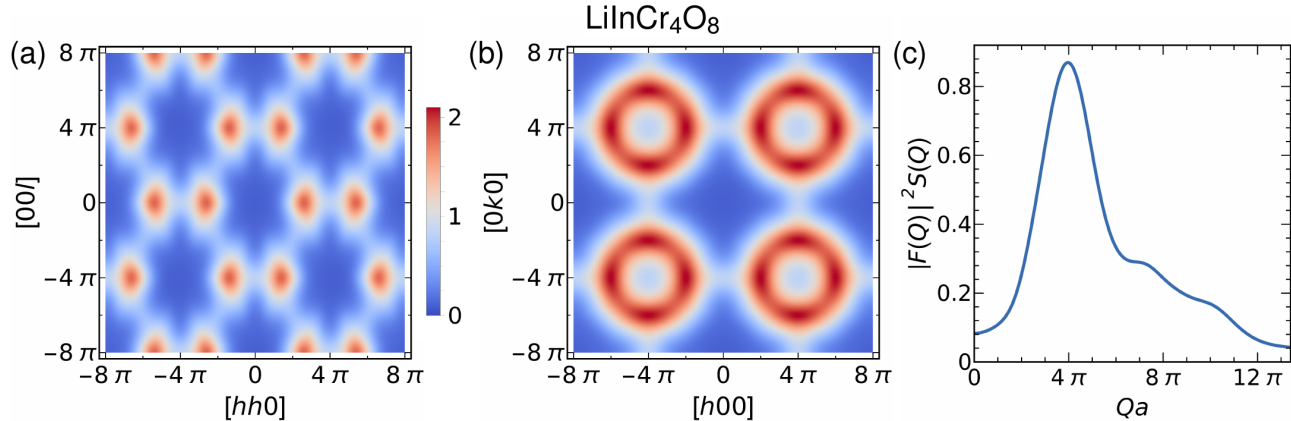


FIG. 4. Spin susceptibility (in units of $1/\bar{J}$) profile for $\text{LiInCr}_4\text{O}_8$ obtained using PFFRG and evaluated at the breakdown point in the RG flow [marked by an arrow in Figure 12], projected on (a) $[hhl]$ -plane and (b) $[hk0]$ -plane. The axes are scaled by a factor of $1/a$, $a = 8.4205$ Å [16]. (c) A plot of the form factor modulated powder averaged susceptibility $|F(Q)|^2 S(Q)$ vs Qa evaluated at the breakdown point in the RG flow for $\text{LiInCr}_4\text{O}_8$.

B. Pseudofermion functional renormalization group calculations

1. Oxides

For $\text{LiInCr}_4\text{O}_8$ and $\text{LiGaCr}_4\text{O}_8$, the J and J' couplings forming the tetrahedra are *both* antiferromagnetic, such that we expect the typical bow-tie features with the associated pinch points in the spin susceptibility (see Ref. [3]). In this previous study, we also show that the inclusion of even very weak second nearest-neighbor couplings can dramatically alter the susceptibility profile of the nearest-neighbor ground state phase and destroy the pinch points and bow-ties [57]. For both the breathing pyrochlore oxides, our DFT analysis reveals the presence of additional antiferromagnetic J_2 , J_{3a} , and J_{3b} couplings. At the classical level, it is known that when the dominant interactions J and J' are large and antiferromagnetic such that the four spins at the vertices of each tetrahedra can be approximated to sum to zero, then a third neighbor coupling J_{3a} in an ideal pyrochlore lattice is equivalent at temperature $T \ll \min(J/k_{\text{B}}, J'/k_{\text{B}})$ to a J_2 coupling with opposite sign [57, 58]. Thus, effectively, both chromium oxides are approximately described by a pyrochlore Hamiltonian with antiferromagnetic J , J' and ferromagnetic J_2 pyrochlore: $(J_2 - J_{3a})/\bar{J} = -0.025$ for $\text{LiInCr}_4\text{O}_8$ and -0.011 for $\text{LiGaCr}_4\text{O}_8$ ($\bar{J} = \sqrt{J^2 + J'^2}$ is the overall nearest-neighbor energy scale, compare Table IV). According to Ref. [3], we expect that the spec-

tral weight moves away from the pinch point and forms two symmetrical lobes, effectively forming a hexagonal cluster pattern of intensities in the $[hhl]$ -plane. Indeed, using the exchange couplings obtained for the room temperature structure, we employ PFFRG to calculate the magnetic susceptibility profiles which are shown in Figures 4 and 5. They are found to closely resemble the susceptibility of the isotropic J_1 - J_2 pyrochlore magnet for antiferromagnetic J_1 and ferromagnetic J_2 [3]. It is worth noting that, due to the relatively weaker effective second nearest-neighbor coupling in $\text{LiGaCr}_4\text{O}_8$, the pinch points and bow-ties are better preserved at low temperature for $\text{LiGaCr}_4\text{O}_8$ [see Figure 5] in comparison to $\text{LiInCr}_4\text{O}_8$ (Figure 4). However, from our PFFRG calculations we find that for both the oxides, and at all temperatures down till the RG flow breakdown point, the maxima of the susceptibility is always located at the high-symmetry W point in the extended Brillouin zone, i.e., at $\mathbf{q} = \frac{2\pi}{a}(2, 1, 0)$ -type ordering vector [see Table V] as found in Ref. [3]. A real-space schematic illustration for the spin configuration corresponding to this order is shown in Figure 6(a). In direct space, for this spin configuration, the pyrochlore lattice decomposes into two pairs of fcc sublattices. Within each pair, the two fcc sublattices are separated from each other by a nearest neighbor vector which is perpendicular to the $\frac{2\pi}{a}$ component of the ordering vector, e.g., for a $\frac{2\pi}{a}(2, 1, 0)$ -ordering vector, one pair of fcc sublattices is separated by the vector $\frac{a}{4}(1, 0, 1)$ and the other pair is

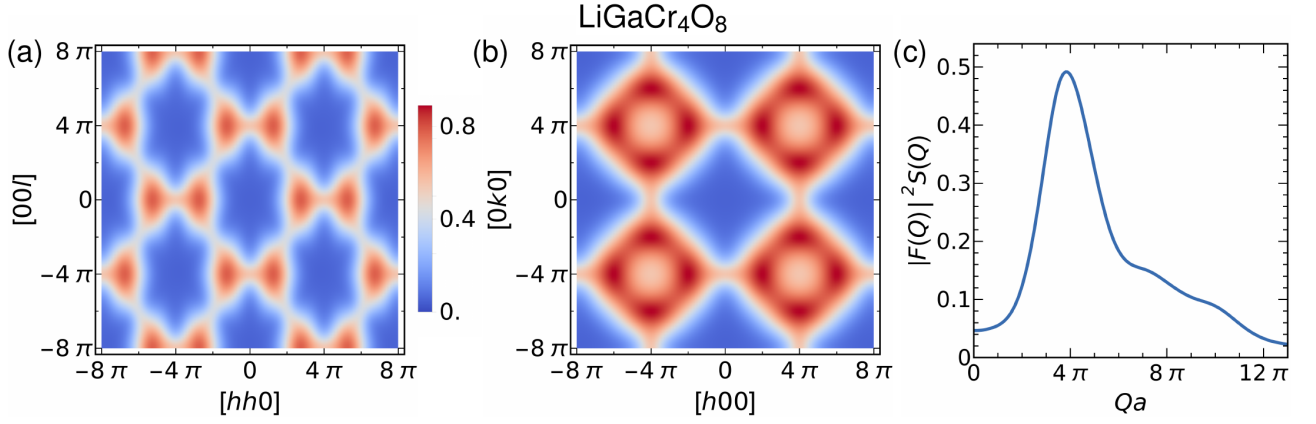


FIG. 5. Spin susceptibility (in units of $1/\bar{J}$) profile for $\text{LiGaCr}_4\text{O}_8$ obtained using PFFRG and evaluated at the breakdown point in the RG flow [marked by an arrow in Figure 12], projected on (a) $[hhl]$ -plane and (b) $[hk0]$ -plane. The axes are scaled by a factor of $1/a$, $a = 8.2551 \text{ \AA}$ [16]. (c) A plot of the form factor modulated powder averaged susceptibility $|F(Q)|^2 S(Q)$ vs Qa at the breakdown point in the RG flow for $\text{LiGaCr}_4\text{O}_8$.

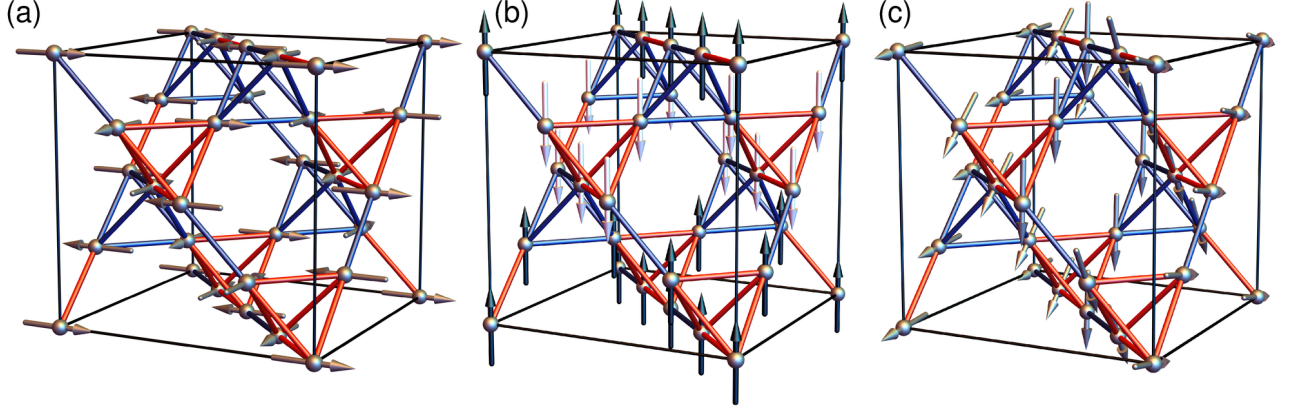


FIG. 6. Ground state spin configurations obtained by iterative minimization, shown in a conventional unit cell of the pyrochlore lattice. (a) $\mathbf{q} = \frac{2\pi}{a}(2, 1, 0)$ order relevant for the oxides $\text{LiInCr}_4\text{O}_8$ and $\text{LiGaCr}_4\text{O}_8$. (b) $\mathbf{q} = \frac{2\pi}{a}(1, 0, 0)$ order relevant for the sulfides $\text{LiInCr}_4\text{S}_8$, $\text{LiGaCr}_4\text{S}_8$ and $\text{CuInCr}_4\text{S}_8$. (c) $(q, 0, 0)$ type planar incommensurate spiral relevant for $\text{CuInCr}_4\text{Se}_8$.

separated by the vector $\frac{a}{4}(1, 0, -1)$. All fcc sublattices show a stripe antiferromagnetic order, i.e., spins are antiferromagnetically aligned in the $\frac{2\pi}{a}$ -direction and ferromagnetically in the perpendicular directions. Within each pair the neighboring spins of different sublattices are aligned antiparallel in spin space. The two pairs can be rotated freely with respect to each other. In reciprocal space, this configuration leads to main Bragg peaks at all $\frac{2\pi}{a}(2, 1, 0)$ -type vectors which share the same $\frac{2\pi}{a}$ component, e.g., $\frac{2\pi}{a}(2, 1, 0)$, $\frac{2\pi}{a}(-2, 1, 0)$, $\frac{2\pi}{a}(0, 1, 2)$, $\frac{2\pi}{a}(0, 1, -2)$, $\frac{2\pi}{a}(2, -1, 0)$, $\frac{2\pi}{a}(-2, -1, 0)$, $\frac{2\pi}{a}(0, -1, 2)$, and $\frac{2\pi}{a}(0, -1, -2)$. In the reciprocal plane perpendicular to the $\frac{2\pi}{a}$ -direction, the relative orientation of the sublattices results in subdominant Bragg peaks with half the intensity of the dominant ones at the $\frac{2\pi}{a}(1, 0, 1)$ -type vectors in this plane, i.e., at $\frac{2\pi}{a}(1, 0, 1)$, $\frac{2\pi}{a}(-1, 0, 1)$, $\frac{2\pi}{a}(1, 0, -1)$, $\frac{2\pi}{a}(-1, 0, -1)$. For the classical model of $\text{LiGaCr}_4\text{O}_8$, this state is the exact ground state given

by the Luttinger-Tisza method and confirmed with iterative minimization. However, we find that this state is strongly dependent on the interplay between the two kinds of third-nearest neighbor couplings. This leads to the finding, that for $\text{LiInCr}_4\text{O}_8$ due to the larger difference between J_{3a} and J_{3b} , an incommensurate order on the sublattices is stabilized as the ground state found by iterative minimization. Note, that the third nearest neighbor couplings and especially their relative size here are the crucial ingredient to stabilize this particular order. Classically, the pure J_1 - J_2 -model on a regular $J = J'$ pyrochlore lattice would feature a $\mathbf{q} = 0$ state, completely different from the $\frac{2\pi}{a}(2, 1, 0)$ -order found here.

The relation $T = (2\pi/3)S(S+1)\Lambda$ can be used to relate the infrared cut-off Λ to temperature T [3], and is obtained by comparing the classical limit ($S \rightarrow \infty$) of PFFRG, where only the RPA diagrams contribute, i.e. a mean-field description, with the conventional spin mean-field theory formulated in terms of temperature T

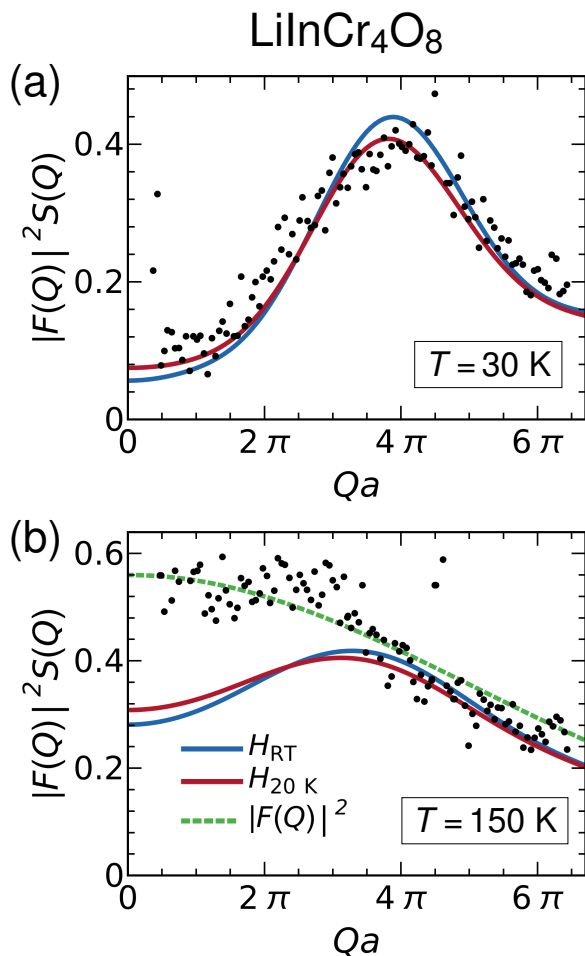


FIG. 7. Comparison (up to a scale factor) between neutron scattering data for $\text{LiInCr}_4\text{O}_8$ and the calculated structure factors $S(Q)$ multiplied with the form factor $|F(Q)|^2$ for Cr^{3+} ions. Black dots are experimental neutron scattering data for a powder sample, taken from Ref. [2]. H_{RT} and $H_{20\text{K}}$ refer to the Hamiltonian parameters calculated for room temperature [see Figure 2(a)] and $T = 20$ K [see Figure 3(a)] structures, respectively.

instead of Λ . The resulting ordering temperatures are given in Table V. As explained in detail in Ref. [3], in the $S \rightarrow \infty$ limit, the absence of higher diagrammatic orders in $1/S$ in the one-loop PFFRG used here implies that, in particular, for the nearest-neighbor pyrochlore antiferromagnetic Heisenberg model, a spurious divergence of the susceptibility at finite temperature occurs which is not expected from what is well established for the classical problem [3, 59]. Thus, our estimates of the ordering temperatures in all of the pyrochlore magnets considered here are systematically overestimated [44]. Our comparisons to an experimental temperature T are shown for a Λ obeying $\Lambda/\Lambda_c = T^{\text{exp}}/T_c^{\text{exp}}$. It is expected that multi-loop implementations of PFFRG will lead to significant improvements for the calculated temperature scales [60], however, this scheme is still under development.

We have also performed the PFFRG calculation for the

$\text{LiInCr}_4\text{O}_8$ Hamiltonian corresponding to its low temperature structure [see Table III]. The calculated susceptibility profile [see Figure 13] is seen to be virtually indistinguishable from that obtained from the room temperature structure shown in Figure 4 even though the breathing anisotropy of the Hamiltonian is significantly different, having evolved from $J'/J = 0.37$ at room temperature to $J'/J = 1$ at $T = 20$ K. The general observation of magnetic response being largely independent of the breathing anisotropy can be understood from a classical picture. As discussed in Appendix C, the eigenvalues of the interaction matrix $\mathcal{J}(\mathbf{k})$ for a J - J' -only model exhibits flat bands at the lowest energies which determine the typical bow-tie features of pyrochlore antiferromagnets. Interestingly, these flat bands persist for any $J > 0$ and $J' > 0$ [2] [see Figure 18], rendering the momentum space profile of the magnetic susceptibility independent of J'/J . As a consequence, longer range J_2 , J_{3a} , J_{3b} are likely to play a crucial role in determining the magnetic behavior of the system. In the present case, however, we find that the effective second-neighbor coupling of $\text{LiInCr}_4\text{O}_8$ at 20 K given by $(J_2 - J_{3a})/\bar{J} = -0.030$ is nearly unchanged compared to room temperature [see Table IV] thus leading to almost identical magnetic responses.

It is now interesting to compare and verify the accuracy of the Hamiltonian determined for $\text{LiInCr}_4\text{O}_8$ against polarized neutron scattering data from powder samples of Okamoto *et al.* [22]. It was shown by Benton *et al.* [2] that within the self-consistent Gaussian approximation, the experimental estimate $J'/J = 0.1$, or even a range $0.05 \lesssim J'/J \lesssim 0.15$, is consistent with the neutron data. Herein, we calculate the product $|F(Q)|^2 S(Q)$ of the magnetic form factor $|F(Q)|^2$ and the powder averaged structure factor $S(Q)$ using

$$F(Q) = -0.3094e^{-0.0274(\frac{Q}{4\pi})^2} + 0.36804e^{-17.0355(\frac{Q}{4\pi})^2} + 0.6559e^{-6.5236(\frac{Q}{4\pi})^2} + 0.2856,$$

for all the materials considered here [61]. In Figure 7 we show the comparison to the $T = 30$ K and the $T = 150$ K neutron scattering data. The DFT determined Hamiltonians for $\text{LiInCr}_4\text{O}_8$ at room temperature ($J'/J = 0.37$) as well as at $T = 20$ K ($J'/J = 1$), upon inclusion of the second- and third-neighbor couplings, give an excellent agreement with the $T = 30$ K neutron data. At $T = 150$ K the neutron data essentially follows the Q dependence of the magnetic form factor [22]; while the computed scattering intensities for the room temperature and $T = 20$ K Hamiltonians are consistent, the disagreement with the experimental $T = 150$ K neutron data is not satisfactory. A similar observation has already been made by Benton *et al.* [2]. We speculate that a possible suppression of magnetic scattering at low angles due to the strong neutron absorption of In [see Table VI] might explain this discrepancy and would be worth further investigating, for example by performing the same experiment on $\text{LiGaCr}_4\text{O}_8$ [62] (Ga has a 70 times smaller

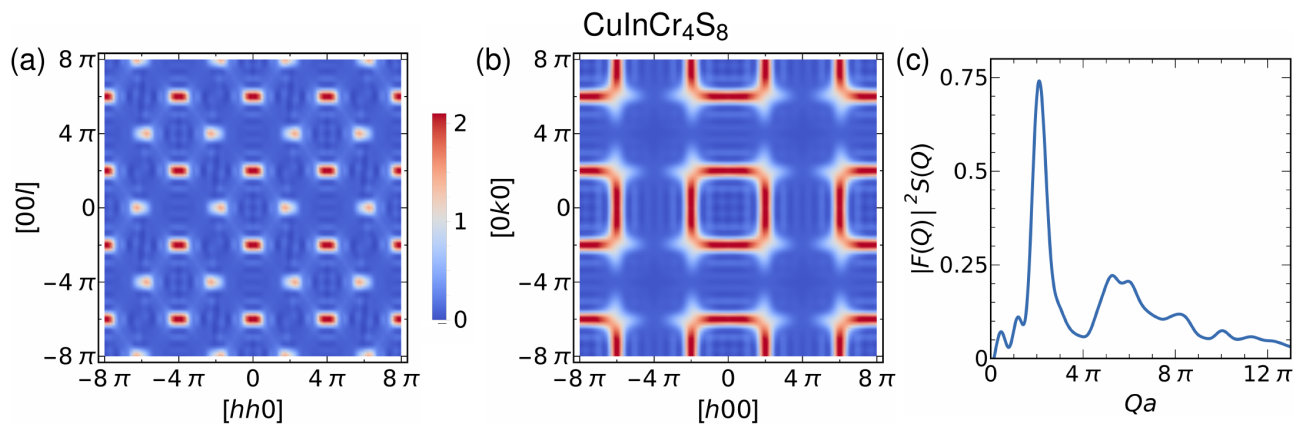


FIG. 8. Spin susceptibility (in units of $1/\bar{J}$) profile for $\text{CuInCr}_4\text{S}_8$ obtained using PFFRG and evaluated at the breakdown point in the RG flow [marked by an arrow in Figure 12], projected on (a) $[hhl]$ -plane and (b) $[hk0]$ -plane. The axes are scaled by a factor of $1/a$, $a = 10.05970 \text{ \AA}$ [34]. (c) A plot of the form factor modulated powder averaged susceptibility $|F(Q)|^2 S(Q)$ vs Qa at the breakdown point in the RG flow.

neutron absorption cross section than In, see Table VI).

2. Sulfides

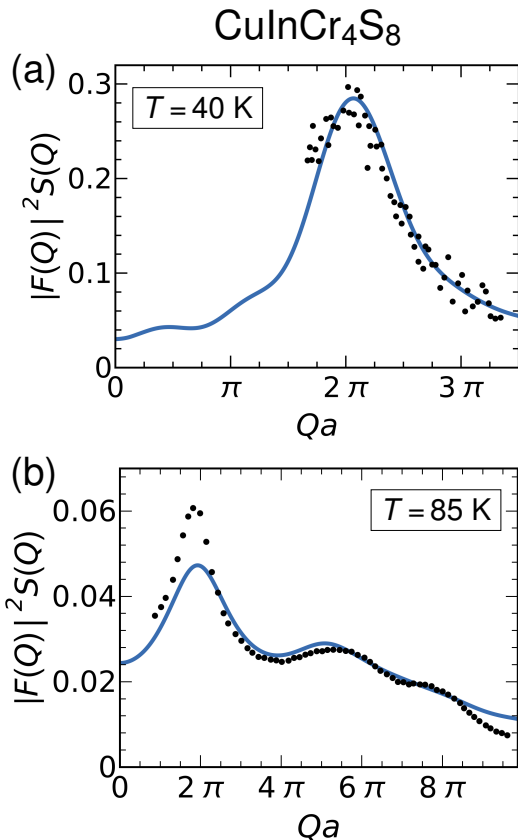


FIG. 9. Plot of $|F(Q)|^2 S(Q)$ vs Qa at (a) 40 K and (b) 85 K for $\text{CuInCr}_4\text{S}_8$ (blue curve). The black dots shows the experimental data obtained by Plumier *et al.* [10, 12].

We have performed PFFRG calculations for all three chromium sulfides, $\text{LiInCr}_4\text{S}_8$, $\text{LiGaCr}_4\text{S}_8$ and $\text{CuInCr}_4\text{S}_8$. As we find very similar susceptibility profiles for the three compounds, we show the one for $\text{CuInCr}_4\text{S}_8$ in Figure 8 and the other two in Appendix B (Figures 14 and 15). $\text{CuInCr}_4\text{S}_8$ has a ferromagnetic J' which is the strongest among all the interactions present in the system. At the low temperatures we are considering here, we can therefore assume that all the spins on the large tetrahedra point in approximately the same direction thereby behaving as effective spin-6 entities. Since the large tetrahedra are arranged in a face centered cubic (fcc) magnetic lattice [see Figure 16], the system can effectively be mapped onto a spin-6 Heisenberg Hamiltonian on a fcc lattice with renormalized nearest-neighbor couplings $J_1^{\text{fcc}} = (J + 4J_2 + 2J_{3a} + 2J_{3b})/16$. These couplings are all antiferromagnetic with values $J_1^{\text{fcc}} = 1.11 \text{ K}$ for $\text{LiInCr}_4\text{S}_8$, $J_1^{\text{fcc}} = 0.95 \text{ K}$ for $\text{LiGaCr}_4\text{S}_8$ and $J_1^{\text{fcc}} = 2.56 \text{ K}$ for $\text{CuInCr}_4\text{S}_8$. Interestingly, the nearest-neighbor antiferromagnetic classical Heisenberg model on the fcc lattice features a subextensive ($\mathcal{O}[L]$) ground state degeneracy in the classical limit ($S \rightarrow \infty$), with the associated wave vectors of the form $\mathbf{q} = \frac{2\pi}{a}(1, \delta, 0)$ and symmetry-related \mathbf{q} [63]. This degeneracy appears as lines of strong intensity in the magnetic response. However, as further explained in Appendix D, the susceptibility profile of our pyrochlore model differs from that of the regular fcc antiferromagnet since it is modulated with a form factor arising from the presence of a tetrahedral basis of our effective fcc lattice. For the structure factors in the $[hk0]$ plane, this leads to a square ring type structure formed by lines of strong and almost constant intensity [2], see Figures 8, 14 and 15. The point $\mathbf{q} = \frac{2\pi}{a}(1, 0, 0)$ (and symmetry-related \mathbf{q} -space positions) is special because it resides at the junctions of the ground state manifold $\mathbf{q} = \frac{2\pi}{a}(1, \delta, 0)$ and $\mathbf{q} = \frac{2\pi}{a}(1, 0, \delta)$. In-

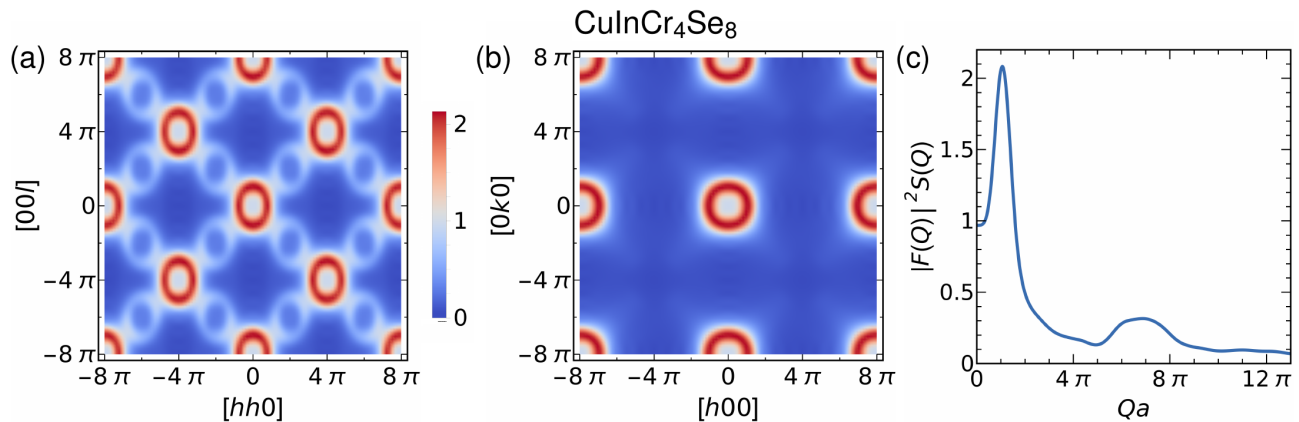


FIG. 10. Spin susceptibility (in units of $1/\bar{J}$) profile for $\text{CuInCr}_4\text{Se}_8$ obtained using PFFRG and evaluated at the breakdown point in the RG flow [marked by an arrow in Figure 12], projected on (a) $[hhl]$ -plane and (b) $[hk0]$ -plane. The axes are scaled by a factor of $1/a$, $a = 10.5735 \text{ \AA}$ [15]. (c) A plot of the form factor modulated powder averaged susceptibility $|F(Q)|^2 S(Q)$ vs Qa at the breakdown point in the RG flow for $\text{CuInCr}_4\text{Se}_8$.

deed, it is found that thermal *order-by-disorder* effects select the collinear ordered states with the ordering wave vector of the type $\mathbf{q} = \frac{2\pi}{a}(1, 0, 0)$ [63, 64]. We investigate the combined selection effect of thermal and quantum fluctuations within PFFRG, and our analysis reveals the appearance of weak maxima at the $\mathbf{q} = \frac{2\pi}{a}(1, 0, 0)$ type positions for all three sulfides [see Table V]. The corresponding real-space spin configuration is illustrated in Figure 6(b). The astonishing property that all sulfides show almost identical susceptibility profiles even though the ratio J_1^{eff}/J' varies significantly between the three compounds can be understood by studying the eigenvalues of the interaction matrix $\mathcal{J}(\mathbf{k})$ for a pyrochlore system with $J > 0$ and $J' < 0$. As shown in Appendix C [see Figure 18], the lowest band exhibits line-like degeneracies regardless of the size of J/J' leading to a magnetic response which is largely independent of this ratio [2].

Plumier *et al.* [10, 12] studied $\text{CuInCr}_4\text{S}_8$ using unpolarized neutrons. In order to compare our calculations to this experiment, we subtract the room temperature neutron spectra from the low temperature spectra, in order to remove the background [62]. In Figure 9, this data is compared to the calculated structure factor weighted with the cross section $|F(Q)|^2 S(Q)$. For the 40 K neutron data, the experiment matches well with our numerical data from PFFRG up to an arbitrary scale factor. At 85 K, the experimental intensity profile does not have as good an agreement for low Q compared to the one at 40 K. This could, in part, be ascribed to the suppression of magnetic scattering at low angles due to the strong neutron absorption of In [see Table VI], and also partly due to the uncertainty in the mapping of the flow parameter Λ to temperature, as explained above. Since, 85 K is about $2.4T_c$ for $\text{CuInCr}_4\text{S}_8$, the calculated structure factor is compared at $2.4\Lambda_c$. The comparison to the available experimental information strongly supports the Hamiltonian we determined for $\text{CuInCr}_4\text{S}_8$.

3. Selenide

The material $\text{CuInCr}_4\text{Se}_8$ is the only available chromium selenide for our study. The Hamiltonian (Table I) at a first glance looks similar to $\text{LiGaCr}_4\text{S}_8$, with a ferromagnetic large tetrahedron. However, the PFFRG result shown in Figure 10 displays a completely different behavior. In contrast to a repetition of the broken high intensity lines representative of one-dimensional sub-extensive degeneracy, we find the two-dimensional degeneracy of a sphere in reciprocal space. Combining all couplings apart from J' into an effective interaction on the large moment fcc lattice, we get a value $J_1^{\text{fcc}} = -0.55 \text{ K}$ which is indicative of the crucial difference between the selenide and the sulfides: nearly negligible J_2 and smaller J_{3a} and J_{3b} couplings do not fully compensate the substantial ferromagnetic J anymore. Nonetheless, clearly no simple ferromagnetic order is realized in $\text{CuInCr}_4\text{Se}_8$. Rather, the two third-neighbor couplings (taken together) substantially perturb the FM tetrahedra which leads to the appearance of a two-dimensional degeneracy of classical ground states. At the ordering temperature (Table V), the system develops an incommensurate spiral magnetic order with a helix pitch vector $\mathbf{q} \approx (0.521, 0, 0)$ (Table V). The corresponding magnetic susceptibility profile obtained from PFFRG at the ordering temperature is shown in Figure 10 wherein one observes peaks in $S(\mathbf{q})$ at $\mathbf{q} \neq \mathbf{0}$. The corresponding direct space spin configuration is illustrated in Figure 6(c). It is worth emphasizing that the shift of the spectral weight away from $\mathbf{q} = \mathbf{0}$ is the combined effect of *both* J_{3a} and J_{3b} couplings of a comparable magnitude [65]. Interestingly, above the ordering temperature, we observe that quantum and thermal fluctuations largely restore the spiral surface, thus suggesting the presence of an approximate spiral spin liquid on the pyrochlore lattice. While an incommensurate spiral phase of $(q, 0, 0)$ type has been observed for the py-

pyrochlore material ZnCr_2Se_4 [65], to the best of our knowledge, the pyrochlore lattice has not been reported to host a spiral spin liquid before.

From a Luttinger-Tisza analysis, the spiral spin surface found in PFFRG is also realized in the classical model. However, the Luttinger-Tisza eigenstates on this spiral surface generically *do not* represent real normalizable spin configurations, i.e., the spin length on different fcc sublattices are not equal in magnitude. It turns out that it is only for the $(q, 0, 0)$ -type ordering vectors that the minimal energy can be achieved by a configuration of normalized spins. The fact that the spiral spin surface despite being present in the classical model is inaccessible at $T = 0$ due to the violation of the spin length constraint does not forbid the possibility of it being accessed via quantum and/or thermal fluctuations. Indeed, for $\text{CuInCr}_4\text{Se}_8$, our PFFRG analysis shows that thermal and quantum fluctuations taken together are able to restore the full spin spiral surface. This single- \mathbf{q} state does not however represent a single planar spiral throughout the entire lattice, instead, similar to what is found in $\text{LiGaCr}_4\text{S}_8$, the lattice can be divided into two pairs of fcc sublattices. Within each pair, the sublattices are connected by a nearest neighbour vector perpendicular to the ordering vector, and the planar spiral orders within each pair are of equal pitch and phase. However, the two pairs of fcc sublattices are found to be out of phase with respect to each other by approximately 5° . This offset in phase is a direct consequence of the breathing anisotropy, and is found to vanish in the isotropic pyrochlore lattice.

IV. DISCUSSION

One of the important findings of this study is the significant role played by long-range exchange interactions on the pyrochlore lattice. While we have previously pointed out the sensitivity of the spin structure factor to the sign and size of the subleading couplings in the J_1 - J_2 pyrochlore Heisenberg antiferromagnet [3], we have found in the chromium breathing pyrochlores an impressive demonstration of the decisive role played by even longer-range couplings, i.e., the two kinds of symmetry inequivalent third-nearest neighbor couplings J_{3a} and J_{3b} . On the other hand, the effects of breathing anisotropy are shown to be surprisingly minor. Indeed, we observe that in $\text{LiInCr}_4\text{O}_8$, the effective ferromagnetic second-neighbor coupling of 2.5% of the average nearest-neighbor coupling far outweighs the substantial breathing anisotropy of $J'/J = 0.37$ in its effect on the structure factor profile. In the case of the sulfides, although the J'/J ratios vary between 93 and -1.8 , the susceptibility profiles appear all very similar. This is rooted in the effective mapping of the system to a nearest-neighbor fcc Heisenberg antiferromagnet with the fcc lattice sites being occupied by ferromagnetic tetrahedra featuring a large $S = 6$ magnetic moment. In this case, we show that the spin structure factor displays line-like degen-

eracies which are largely independent of the breathing anisotropy ratio J'/J . Finally, for the dominantly ferromagnetic selenide $\text{CuInCr}_4\text{Se}_8$ we demonstrate that the combined effect of the two third-neighbor couplings perturbs the ground state away from the simple ferromagnetic order. Interestingly, we find that the perturbed state corresponds to an approximate spiral spin liquid above the ordering temperature, where the individual wave vectors form a sphere-like manifold in reciprocal space. Our PFFRG analysis indicates that the combined effect of quantum and thermal fluctuations only leads to a weak order-by-disorder selection into an incommensurate spiral state. Approximate spiral spin liquids on three-dimensional lattices are so far known only on the diamond lattice in MnSc_2S_4 [44, 66, 67].

V. CONCLUSION

We have theoretically investigated six chromium spinels featuring breathing anisotropy. The Hamiltonians which were determined from first principles density functional theory calculations and investigated using the pseudofermion functional renormalization group method showcase a colorful selection of pyrochlore magnetic properties. We find that the oxide compounds are in a perturbed Coulomb phase, reminiscent of the famous spin ice materials. The sulfides display an effective fcc lattice Heisenberg antiferromagnetic type behavior, and the selenide features incommensurate magnetic correlations. As a unifying feature, all materials are found to be close to a classical degeneracy which shows up in different variants: The oxides are near a phase with a classical spin ice degeneracy featuring an extensive number of ground states scaling exponentially in the volume of the system. The selenide is approximately degenerate on a two-dimensional surface with a manifold of states scaling exponentially in L^2 (where L is the linear dimension of the system). Finally, the sulfides are characterized by approximate line-like degeneracies with the number of ground states scaling exponentially in the linear dimension L . This variety of different behaviors in a family of related materials represent an attractive feature which promises a wealth of future investigations particularly experimental investigations with single-crystals which will allow to assess our theoretical predictions.

ACKNOWLEDGMENTS

We thank Zenji Hiroi, Gran Nilsen, Yoshihiko Okamoto, Owen Benton, Hikaru Kawamura and Jason Gardner for useful discussions. We gratefully acknowledge the Gauss Centre for Supercomputing e.V. for funding this project by providing computing time on the GCS Supercomputer SuperMUC at Leibniz Supercomputing Centre (LRZ). P.G., Y.I., and T.M. acknowledge the interactions and kind hospitality at the International

Centre for Theoretical Sciences (ICTS), Bengaluru, India from 29th November till 7 December, 2018 during “The 2nd Asia Pacific Workshop on Quantum Magnetism”. J.R. acknowledges the kind hospitality of the Indian Institute of Technology Madras, Chennai, India where this work was completed. The work at the University of Waterloo was supported by the Canada Research Chair program (M.J.P.G., Tier 1).

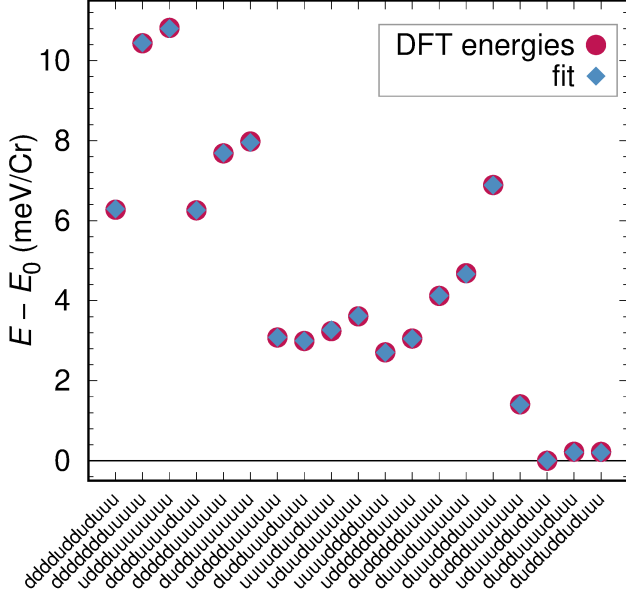


FIG. 11. Density functional theory energies for 19 different spin configurations of $\text{LiInCr}_4\text{O}_8$ calculated with GGA+ U exchange correlation functional at $U = 2$ eV and $J_{\text{H}} = 0.72$ eV. The fit to the Heisenberg Hamiltonian with six exchange couplings is very good.

Appendix A: Additional DFT details

Energy mapping for the chromium breathing pyrochlores works very well. Total moments are exact multiples of $3 \mu_{\text{B}}$ as all chromium moments are exactly $S = 3/2$. All fits are extremely good; an example is given in Figure 11.

For convenience, we show in Table IV the average nearest-neighbor energy scale $\bar{J} = \sqrt{J^2 + J'^2}$ for all compounds and all temperatures discussed in the main text (see Tables I and III) as well as the relative strength of the longer range couplings with respect to this scale. The last column contains the relative combined strength of J_2 and J_{3a} which are, at the classical level, equivalent (with opposite sign) on the ideal pyrochlore lattice [57, 58].

Appendix B: Additional PFFRG data

In the PFFRG approach, the onset of magnetic long-range order is signaled by a breakdown of the smooth

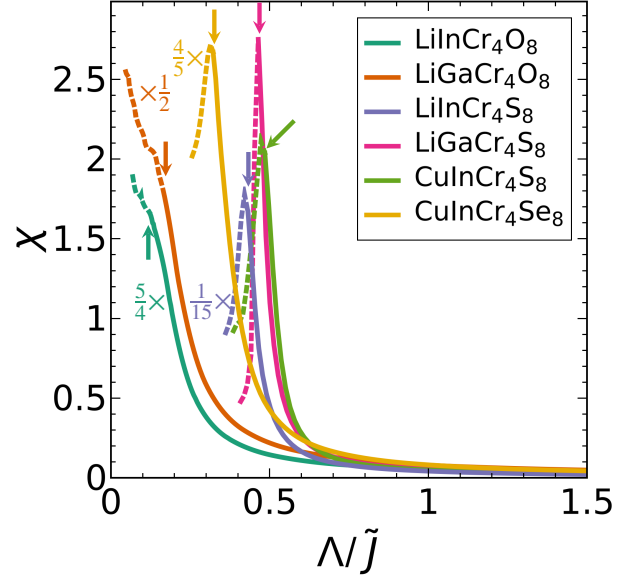


FIG. 12. RG flows of the maximum of magnetic susceptibilities of all the six compounds under investigation. The points at which the solid lines become dashed indicate an instability in the flow and express the onset of a magnetic order.

renormalization group flow. Figure 12 shows the flows computed for the room temperature structures of all six breathing pyrochlore compounds considered in this study. The continuation of the flow below the breakdown energy scale is shown with a dashed line as the PFFRG calculation becomes less reliable in the ordered state. The ordering temperatures determined in this way are shown in Table V together with the ordering wave vectors.

Oxides.- The room temperature susceptibility profiles of $\text{LiInCr}_4\text{O}_8$ is shown in the main text (see Figure 4). The PFFRG calculation with the low temperature structure of $\text{LiInCr}_4\text{O}_8$ yields the susceptibility profiles shown in Figure 13; it is calculated with the $T = 20$ K Hamiltonian parameters from Table III. Even though the breathing anisotropy is reduced from $J'/J = 0.37$ to $J'/J = 1$, the two static spin susceptibility profiles are very similar.

The neutron absorption cross section of In and Ga are given in Table VI. A possible reason for the mismatch between polarized neutron scattering data for $\text{LiInCr}_4\text{O}_8$ at $T = 150$ K and both classical [2] and PFFRG calculations (Figure 7 (b)) is that the element In has a very high neutron absorption cross section [62].

Sulfides.- The spin susceptibility profile of $\text{LiGaCr}_4\text{S}_8$ is shown in the main text (see Figure 8). The other two sulfide spin susceptibility profiles are shown in Figures 14 and 15. All three sulfide PFFRG results are rather similar even though the Hamiltonians do not appear very similar. As explained in the main text, this can be understood by recognizing that the ferromagnetic large tetrahedra form an fcc lattice of large $S = 6$ magnetic mo-

TABLE IV. Longer range exchange couplings of the chromium breathing pyrochlore compounds, relative to the average nearest-neighbor energy scale $\bar{J} = \sqrt{J^2 + J'^2}$. The absolute numbers are given in Tables I and III.

| Material | T (K) | \bar{J} (K) | J_2/\bar{J} | J_{3a}/\bar{J} | J_{3b}/\bar{J} | $(J_2 - J_{3a})/\bar{J}$ |
|-------------------------------------|---------|---------------|---------------|------------------|------------------|--------------------------|
| LiInCr ₄ O ₈ | 20 | 57.5 | 0.006 | 0.035 | 0.016 | -0.030 |
| LiInCr ₄ O ₈ | RT | 63.7 | 0.004 | 0.029 | 0.015 | -0.025 |
| LiGaCr ₄ O ₈ | RT | 120.0 | 0.006 | 0.016 | 0.011 | -0.011 |
| LiInCr ₄ S ₈ | RT | 27.8 | 0.025 | 0.190 | 0.086 | -0.165 |
| LiGaCr ₄ S ₈ | 10 | 14.3 | 0.083 | 0.432 | 0.215 | -0.350 |
| LiGaCr ₄ S ₈ | RT | 14.4 | 0.081 | 0.422 | 0.210 | -0.341 |
| CuInCr ₄ S ₈ | RT | 29.6 | 0.038 | 0.215 | 0.153 | -0.177 |
| CuInCr ₄ Se ₈ | RT | 40.1 | 0.008 | 0.117 | 0.094 | -0.109 |

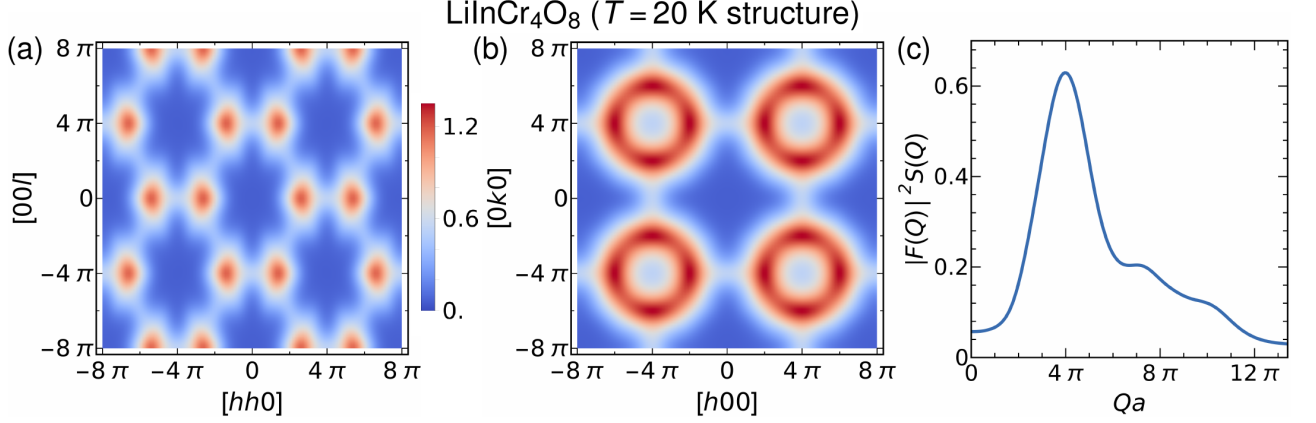


FIG. 13. Spin susceptibility profile for the $T = 20$ K Hamiltonian of LiInCr₄O₈ obtained using PFFRG at the breakdown, projected on (a) $[hhl]$ and (b) $[hk0]$ planes. The axes are scaled by a factor of $1/a$, $a = 8.40347$ Å [18]. (c) Plot of $|F(Q)|^2 S(Q)$ vs Qa at the breakdown for LiInCr₄O₈.

| | $\mathbf{q}(2\pi/a)$ | T_c (K) (PFFRG) | T_c (K) (experimental) |
|-------------------------------------|----------------------|----------------------|-----------------------------|
| LiInCr ₄ O ₈ | (2, 1, 0) | 60.6 | 15.9 [16] |
| LiGaCr ₄ O ₈ | (2, 1, 0) | 159.8 | 13.8 [16] |
| LiInCr ₄ S ₈ | (1, 0, 0) | 95.0 | 24 [34] |
| LiGaCr ₄ S ₈ | (1, 0, 0) | 49.1 | 10 [33, 34] |
| CuInCr ₄ S ₈ | (1, 0, 0) | 114.7 | 40 [10], 35 [12], 32 [34] |
| CuInCr ₄ Se ₈ | (0.521, 0, 0) | 99.3 | 14 [7] |

TABLE V. PFFRG results for the magnetic ordering in the six chromium breathing pyrochlore spinels. The second column shows the ordering wave vector, and third and fourth columns compare PFFRG estimates of ordering temperatures with experimental T_N or T_c values.

ments, as illustrated in Figure 16 (a). The renormalized nearest-neighbor interactions in the fcc lattice is given by $J_1^{\text{fcc}} = (J + 4J_2 + 2J_{3a} + 2J_{3b})/16$ as can be read off from Figure 16 (b). For the three sulfides, J_1^{fcc} turns out to be antiferromagnetic.

In the main text, we show that the form factor modulated powder averaged susceptibility $|F(Q)|^2 S(Q)$ which we calculated for CuInCr₄S₈ matches the experimental data of Ref. [10, 12] very well, accurately reproducing three peak positions at $T = 85$ K. We would like to

| | σ_S | σ_A |
|----|------------|------------|
| In | 2.62 | 193.8(1.5) |
| Ga | 6.83 | 2.75 |

TABLE VI. The neutron cross section (in barns) data of In and Ga as given in Ref. [70]: Scattering cross section σ_S and absorption cross section σ_A .

investigation the question to what extent the subleading exchange couplings are important for this very good agreement. Therefore, we calculate the $|F(Q)|^2 S(Q)$ for Hamiltonians where we set selected longer range couplings to zero; we consider the set J - J' - J_2 (J_{3a} and J_{3b} are neglected), the set J - J' - J_2 - J_{3a} (J_{3b} is neglected) and the set J - J' - J_2 - J_{3b} (J_{3a} is neglected). The result is shown in Figure 17. From both the plots, it becomes very clear that the best match with the experimental data is only obtained only with the full J - J' - J_2 - J_{3a} - J_{3b} model. Each omission of a subleading coupling leads to a worse match with experiment. This validates the values we determined for CuInCr₄S₈ using DFT energy mapping and underlines the crucial role played by the subleading couplings up to third nearest neighbor in the breathing pyrochlores.

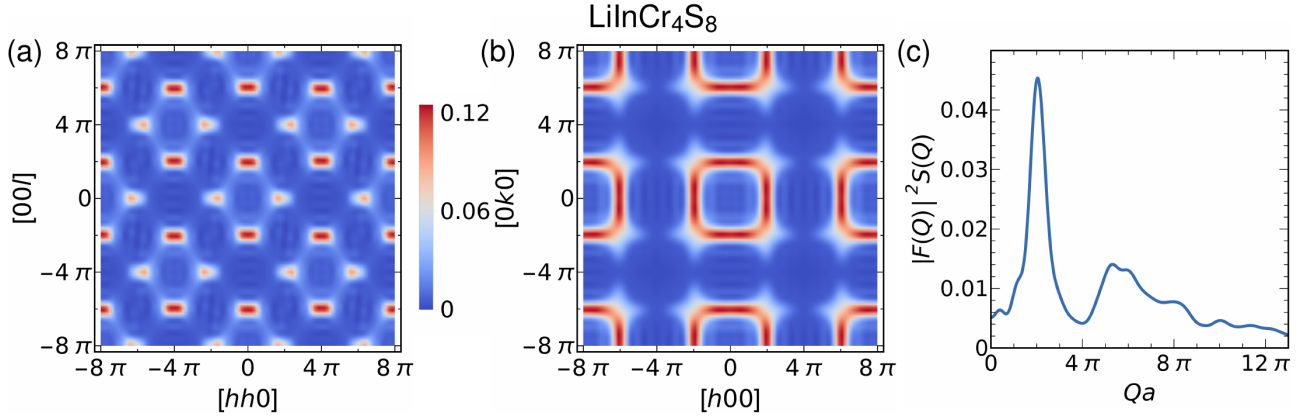


FIG. 14. Spin susceptibility profile for $\text{LiInCr}_4\text{S}_8$ obtained using PFFRG at the breakdown, projected on (a) $[hhl]$ and (b) $[hk0]$ planes. The axes are scaled by a factor of $1/a$, $a = 10.13210 \text{ \AA}$ [34]. (c) Plot of $|F(Q)|^2 S(Q)$ vs Qa at the breakdown for $\text{LiInCr}_4\text{S}_8$.

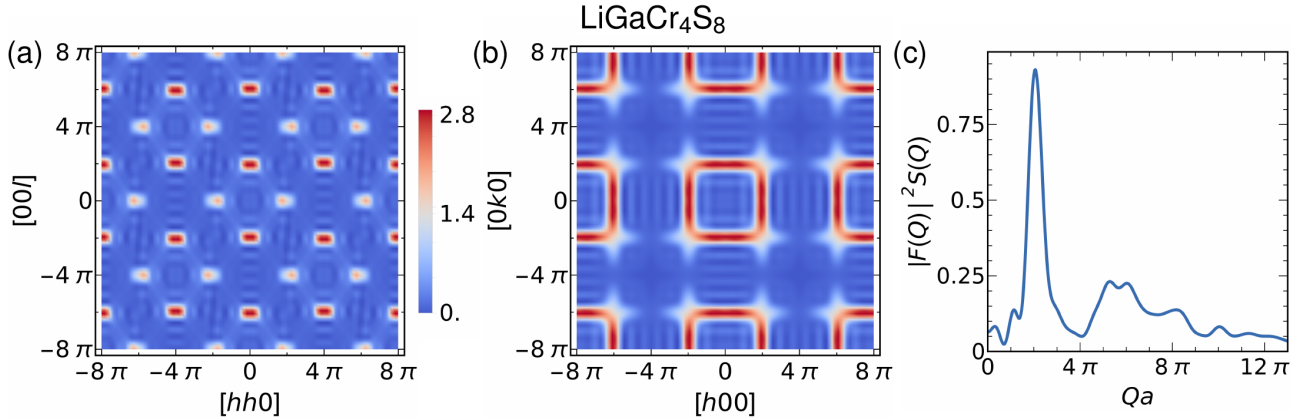


FIG. 15. Spin susceptibility profile for $\text{LiGaCr}_4\text{S}_8$ obtained using PFFRG at the breakdown, projected on (a) $[hhl]$ and (b) $[hk0]$ planes. The axes are scaled by a factor of $1/a$, $a = 9.96593 \text{ \AA}$ [34]. (c) Plot of $|F(Q)|^2 S(Q)$ vs Qa at the breakdown for $\text{LiGaCr}_4\text{S}_8$.

Appendix C: Luttinger-Tisza calculations

We employ the Luttinger-Tisza method [54, 68, 69] to better understand the classical ground states of the breathing pyrochlore Hamiltonians. Figure 18 shows the evolution of the eigenvalues of the Luttinger-Tisza matrix for various breathing anisotropies J'/J . The minimum of the resulting bands identifies the ordering vector of the classical Hamiltonian in reciprocal space. The minima can also be degenerate, and the method allows us to identify one-, two- or even three-dimensional classical degeneracies of the ground state manifold.

Relevant for the chromium oxide spinels, Figure 18 (a) to (d) shows the eigenvalues for antiferromagnetic J and J' . The lowest Luttinger-Tisza band is completely flat, indicating a three-dimensional manifold of degenerate ground states. Decreasing J as compared to J' in Figures 18 (b), (c) and (d) only shrinks the band width but does not lift the degeneracy of the lowest band. This explains why the typical bow-tie pattern in the magnetic

susceptibility is nearly independent on the J'/J ratio.

For a better understanding of the chromium sulfide spinels, Figure 18 (e) to (h) shows the case of a ferromagnetic large tetrahedron J' together with several antiferromagnetic J values. In this case, the minima of the lowest Luttinger-Tisza band form the lines marked in red. The ground state has a one-dimensional sub-extensive degeneracy. Again, this degeneracy is independent of the value of the J'/J ratio. This explains why the three sulfides show very similar susceptibilities even though their Hamiltonians appear at first sight rather diverse.

Appendix D: Basis effects in the structure factor

We investigate the origin of the calculated susceptibilities of the chromium sulfides shown in Figures 8, 14 and 15. For this purpose, we use the Luttinger-Tisza method [54, 68, 69] to solve the antiferromagnetic Heisenberg Hamiltonian on the fcc lattice. The result is shown

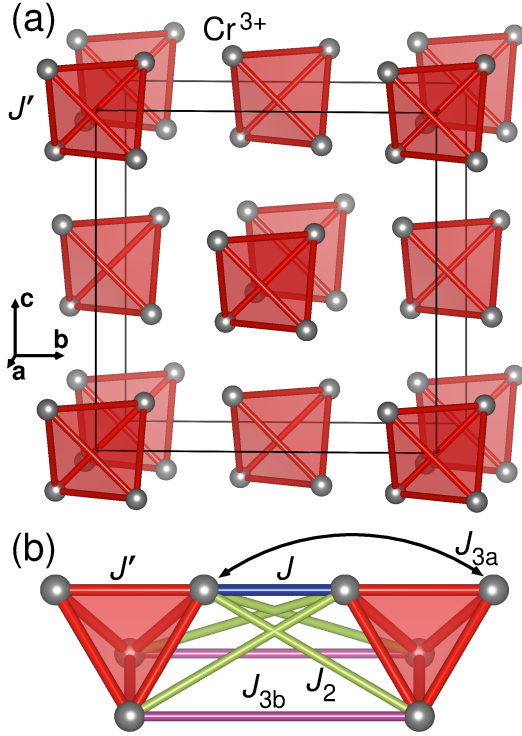


FIG. 16. (a) Effective face centered cubic lattice formed by the large tetrahedra of the chromium sulfides. Only the strong ferromagnetic J' coupling is depicted which turns the Cr^{3+} tetrahedra into approximate $S = 6$ units. (b) Exchange interactions between nearest-neighbor large tetrahedra in the fcc structure.

in Figure 19(a). Now, we have to take into account the fact that the classical $S = 6$ magnetic moment on the fcc lattice is not point-like and instead has an internal structure – the moment being composed of six $S = 3/2$ moments arranged on a tetrahedron constituting a basis. Thus, the complete structure factor of the pyrochlore lattice is now determined by multiplying the spin structure factor on the fcc lattice with the square of the absolute value of the Fourier transform of the magnetic basis

$$f(\mathbf{q}) = \frac{1}{4} \left(1 + e^{-i\frac{a}{4}(q_x+q_y)} + e^{-i\frac{a}{4}(q_x+q_z)} + e^{-i\frac{a}{4}(q_y+q_z)} \right). \quad (\text{D1})$$

The susceptibility profiles therefore acquire a factor of $|f(\mathbf{q})|^2$ between fcc and pyrochlore lattice:

$$S_{\text{Pyro}}(\mathbf{q}) = |f(\mathbf{q})|^2 S_{\text{fcc}}(\mathbf{q}). \quad (\text{D2})$$

The classical spin susceptibility of a fcc nearest-neighbor Heisenberg antiferromagnet, relevant to the sulfides [see Sec. III B 2] consists of degenerate maxima in the $[hk0]$ planes along the lines $\mathbf{q} = \frac{2\pi}{a}(\pm n, \delta, 0)$ and $\mathbf{q} =$

$\frac{2\pi}{a}(\delta, \pm n, 0)$, which form edge sharing squares with side length $4\pi/a$ in reciprocal space, as shown in figure 19(a). The factor $|f(\mathbf{q})|^2$, shown in 19(b) is 1 at $(0, 0, 0)$, and zero at on the lines $\mathbf{q} = \frac{4\pi}{a}(\pm n, \delta, 0)$ and $\mathbf{q} = \frac{4\pi}{a}(\delta, \pm n, 0)$, and thus 8π periodic. This implies every second row and

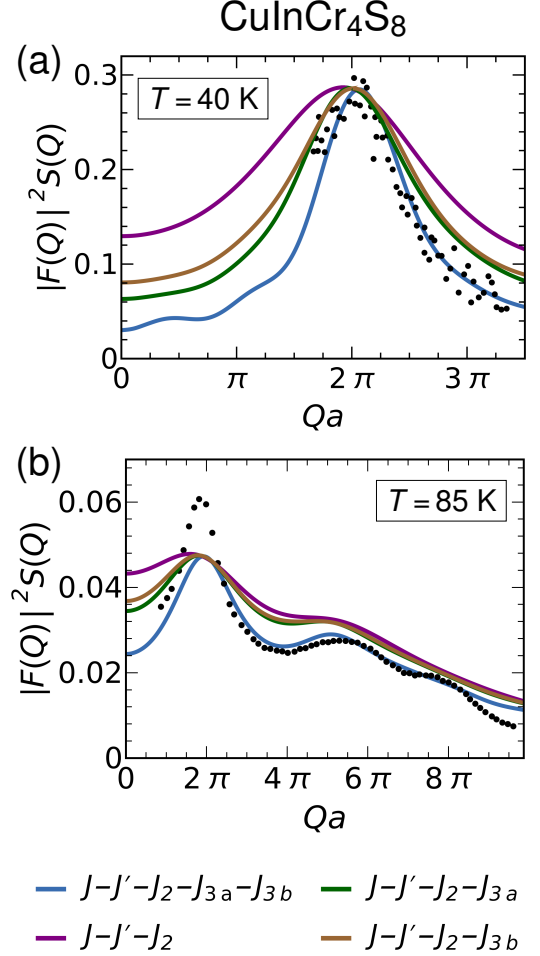


FIG. 17. The comparison of $|F(Q)|^2 S(Q)$ for different combinations of $J, J', J_2, J_{3a}, J_{3b}$ with the experimental data obtained by Plumier *et al.* [12] at (a) 40K and (b) 85K for $\text{CuInCr}_4\text{S}_8$. The experimental data is shown in red dots. From both the plots, it is very evident that the best match with the experimental data is only obtained only with the full $J-J'-J_2-J_{3a}-J_{3b}$ model. This validates the value of exchange couplings used in our calculations regarding $\text{CuInCr}_4\text{S}_8$.

column of squares in the fcc susceptibility is suppressed by the sublattice structure [see Figure 19 (c)], this giving rise to a pattern of disconnected squares of maxima on the pyrochlore lattice which are also modulated in their intensity. Indeed, this is precisely what PFFRG finds for the chromium sulfide breathing pyrochlores [see Figures 8, 14 and 15].

[1] J. S. Gardner, M. J. P. Gingras, J. E. Greedan, Magnetic pyrochlore oxides, Rev. Mod. Phys. **82**, 53 (2010).

[2] O. Benton, N. Shannon, Ground State Selection and Spin-Liquid Behaviour in the Classical Heisenberg Model

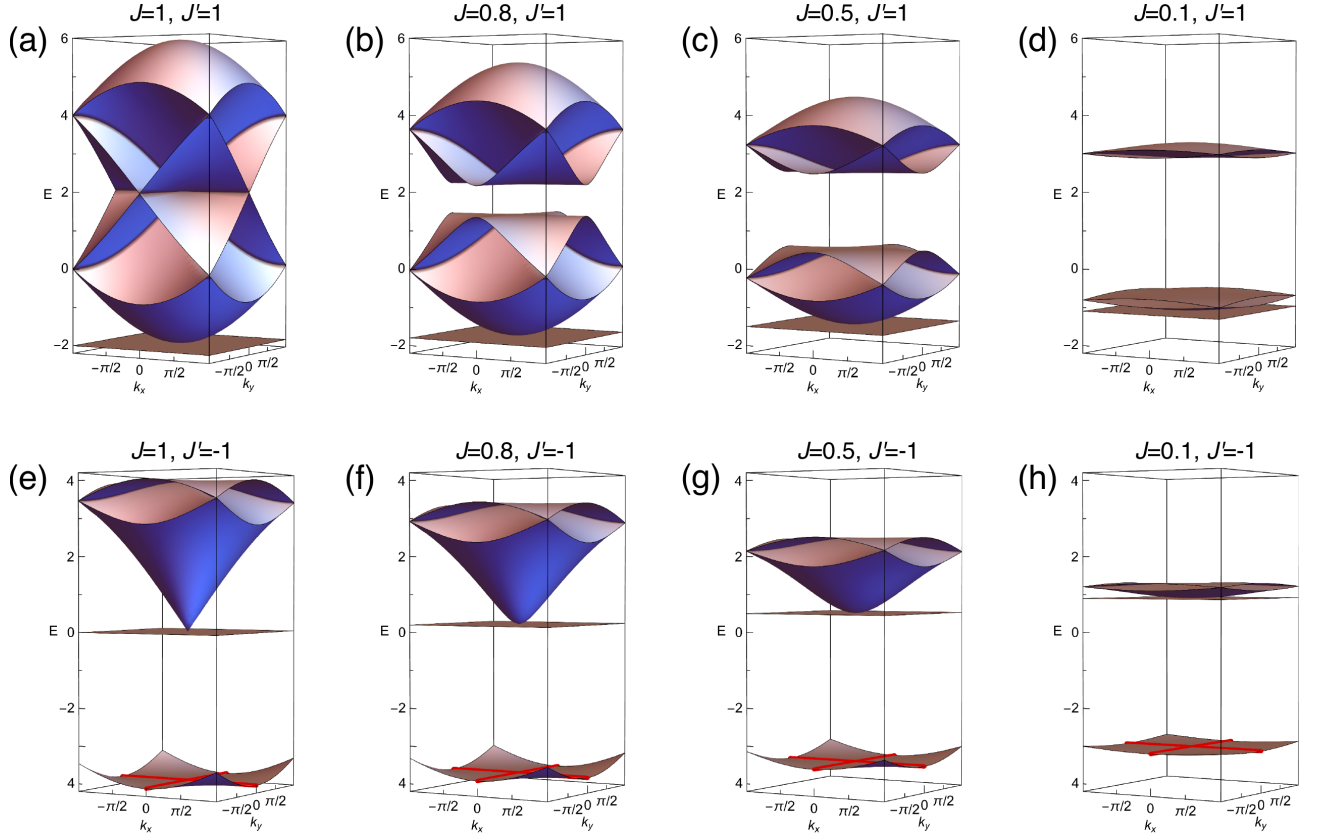


FIG. 18. Eigenvalues of the Luttinger-Tisza matrix for the breathing pyrochlore Hamiltonian with nearest-neighbor exchanges J and J' . (a)-(d) Antiferromagnetic case for constant $J' = 1$ and decreasing J . (e)-(h) Ferromagnetic $J' = -1$ with decreasing antiferromagnetic J . All plots show the $(h, k, 0)$ plane, with k_z chosen to be zero.

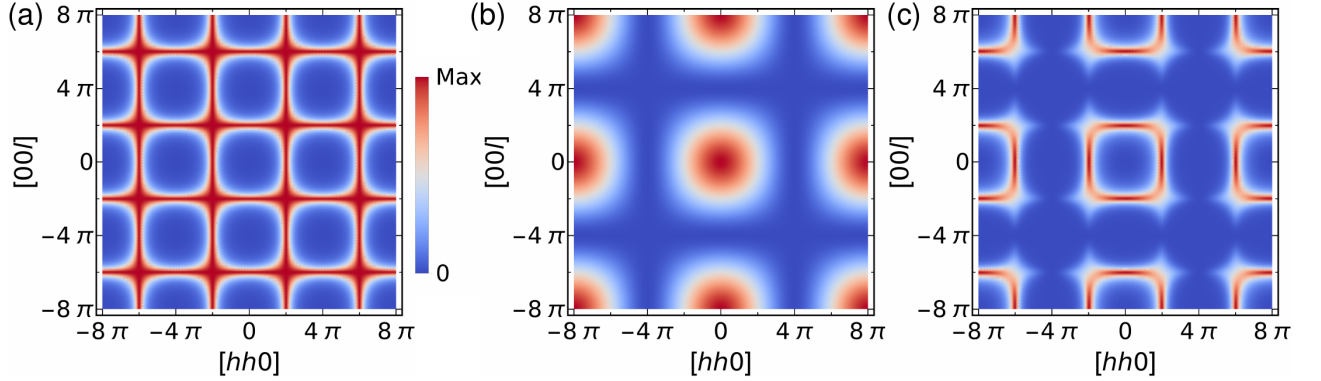


FIG. 19. Inclusion of the pyrochlore basis in an fcc structure factor. (a) Classical spin susceptibility of the fcc nearest-neighbor Heisenberg antiferromagnet just above the ordering temperature. (b) Structure factor $|f(\mathbf{q})|^2$ of the pyrochlore basis. (c) Classical spin susceptibility of an effective fcc nearest-neighbor model on the pyrochlore lattice formed by ferromagnetically ordered tetrahedra [see Figure 16], given by the product of (a) and (b).

on the Breathing Pyrochlore Lattice, *J. Phys. Soc. Jpn.* **84**, 104710 (2015).

- [3] Y. Iqbal, T. Müller, P. Ghosh, M. J. P. Gingras, H. O. Jeschke, S. Rachel, J. Reuther, and R. Thomale, Quantum and Classical Phases of the Pyrochlore Heisenberg Model 3 with Competing Interactions, *Phys. Rev. X* **9**, 011005 (2019).

- [4] J.-C. Joubert, A. Durif, Étude de quelques composés spinelles nouveaux possédant un ordre des cations du type 1/1 sur les sites tétraédriques, *Bull. Soc. Fr. Mineral. Cristallogr.* **89**, 26 (1966).

- [5] H. Haeuseler and H. D. Lutz, Gitterschwingungsspektren XVIII. Chromthio- und Chromselenospinelle mit 1:1-Ordnung auf den Tetraederplätzen, *J. Solid State*

- Chem. **22**, 201 (1977).
- [6] F. K. Lotgering, R. P. van Stapele, G.H.A.M. van der Steen and J. S. van Wieringen, Magnetic properties, conductivity and ionic ordering in $\text{Fe}_{1-x}\text{Cu}_x\text{Cr}_2\text{S}_4$, J. Phys. Chem. Solids **30**, 799 (1969).
- [7] H. L. Pinch, M. J. Woods, and E. Lopatin, Some new mixed A-site chromium chalcogenide spinels, Mat. Res. Bull. **5**, 425 (1970).
- [8] S.-H. Lee, H. Takagi, D. Louca, M. Matsuda, S. Ji, H. Ueda, Y. Ueda, T. Katsufuji, J.-H. Chung, S. Park, S.-W. Cheong, and C. Broholm, Frustrated Magnetism and Cooperative Phase Transitions in Spinel, J. Phys. Soc. Jpn. **79**, 011004 (2010).
- [9] H. Yokoyama, S. Chiba, Preparation and Magnetic Properties of a New Selenide Spinel $\text{Cu}_{1/2}\text{In}_{1/2}\text{Cr}_2\text{Se}_4$, J. Phys. Soc. Jpn. **27**, 505 (1969).
- [10] R. Plumier, F. K. Lotgering, R. P. van Stapele, Magnetic properties of $\text{Cu}_{1/2}\text{In}_{1/2}\text{Cr}_2\text{S}_4$ and some related compounds, J. Phys. Colloques **32**, C1-324 (1971).
- [11] W. K. Unger, H. Göbel, L. Treitinger and H. Pink, Magnetic susceptibility of semiconducting $\text{Cu}_{1-x}\text{In}_x\text{Cr}_2\text{S}_4$ spinels, Physica **80B**, 62 (1975).
- [12] R. Plumier, M. Sougi and M. Lecomte, Observation of an unusual short range magnetic ordering in spinel $\text{Cu}_{1/2}\text{In}_{1/2}\text{Cr}_2\text{S}_4$, Phys. Lett. **60A**, 431 (1977).
- [13] R. Plumier, M. Sougi, M. Lecomte, and A. Miedan-Gros, High Magnetic Field Study of Sulphur Spinel $\text{Cu}_{1/2}\text{In}_{1/2}\text{Cr}_2\text{S}_4$, Z. Phys. B Condens. Matter **40**, 227 (1980).
- [14] R. Plumier and M. Sougi, Magnetic ordering in the normal spinel $\text{Cu}_{0.5}\text{In}_{0.5}\text{Cr}_2\text{Se}_4$, Solid State Commun. **69**, 341 (1989).
- [15] H. Duda, E. Maciazek, T. Gron, S. Mazur, A. W. Pacyna, A. Waskowska, T. Mydlarz, and A. Gilewski, Spin-glass-like behavior in single-crystalline $\text{Cu}_{0.44}\text{In}_{0.48}\text{Cr}_{1.95}\text{Se}_4$, B **77**, 035207 (2008).
- [16] Y. Okamoto, G. J. Nilsen, J. P. Attfield, and Z. Hiroi, Breathing Pyrochlore Lattice Realized in A-Site Ordered Spinel Oxides $\text{LiGaCr}_4\text{O}_8$ and $\text{LiInCr}_4\text{O}_8$, Phys. Rev. Lett. **110**, 097203 (2013).
- [17] Y. Tanaka, M. Yoshida, M. Takigawa, Y. Okamoto, and Z. Hiroi, Novel Phase Transitions in the Breathing Pyrochlore Lattice: ^7Li -NMR on $\text{LiInCr}_4\text{O}_8$ and $\text{LiGaCr}_4\text{O}_8$, Phys. Rev. Lett. **113**, 227204 (2014).
- [18] G. J. Nilsen, Y. Okamoto, T. Masuda, J. Rodriguez-Carvajal, H. Mutka, T. Hansen, and Z. Hiroi, Complex magnetostructural order in the frustrated spinel $\text{LiInCr}_4\text{O}_8$, Phys. Rev. B **91**, 174435 (2015).
- [19] S. Lee, S.-H. Do, W.-J. Lee, Y. S. Choi, M. Lee, E. S. Choi, A. P. Reyes, P. L. Kuhns, A. Ozarowski, and K.-Y. Choi, Multistage symmetry breaking in the breathing pyrochlore lattice $\text{Li}(\text{Ga}_1\text{n})\text{Cr}_4\text{O}_8$, Phys. Rev. B **93**, 174402 (2016).
- [20] R. Saha, F. Fauth, M. Avdeev, P. Kayser, B. J. Kennedy, and A. Sundaresan, Magnetodielectric effects in A-site cation-ordered chromate spinels LiMCr_4O_8 ($M = \text{Ga}$ and In), Phys. Rev. B **94**, 064420 (2016).
- [21] Y. Okamoto, D. Nakamura, A. Miyake, S. Takeyama, M. Tokunaga, A. Matsuo, K. Kindo, and Z. Hiroi, Magnetic transitions under ultrahigh magnetic fields of up to 130 T in the breathing pyrochlore antiferromagnet $\text{LiInCr}_4\text{O}_8$, Phys. Rev. B **95**, 134438 (2017).
- [22] Y. Okamoto, G. J. Nilsen, T. Nakazono, and Z. Hiroi, Magnetic Phase Diagram of the Breathing Pyrochlore Antiferromagnet $\text{LiGa}_{1-x}\text{In}_x\text{Cr}_4\text{O}_8$, J. Phys. Soc. Jpn. **84**, 043707 (2015).
- [23] R. Wawrzyńczak, Y. Tanaka, M. Yoshida, Y. Okamoto, P. Manuel, N. Casati, Z. Hiroi, M. Takigawa, and G. J. Nilsen, Classical Spin Nematic Transition in $\text{LiGa}_{0.95}\text{In}_{0.05}\text{Cr}_4\text{O}_8$, Phys. Rev. Lett. **119**, 087201 (2017).
- [24] Y. Tanaka, R. Wawrzyńczak, M. D. Le, T. Guidi, Y. Okamoto, T. Yajima, Z. Hiroi, M. Takigawa, and G. J. Nilsen, Inelastic Neutron Scattering Study of the Spin Dynamics in the Breathing Pyrochlore System $\text{LiGa}_{0.95}\text{In}_{0.05}\text{Cr}_4\text{O}_8$, J. Phys. Soc. Jpn. **87**, 073710 (2018).
- [25] H. Tsunetsugu, Theory of antiferromagnetic Heisenberg spins on a breathing pyrochlore lattice, Prog. Theor. Exp. Phys. **2017**, 033101.
- [26] K. Aoyama and H. Kawamura, Spin-Lattice-Coupled Order in Heisenberg Antiferromagnets on the Pyrochlore Lattice, Phys. Rev. Lett. **116**, 257201 (2016).
- [27] K. Aoyama and H. Kawamura, Spin ordering induced by lattice distortions in classical Heisenberg antiferromagnets on the breathing pyrochlore lattice, arXiv:1901.05098.
- [28] F.-Y. Li, Y.-D. Li, Y. B. Kim, L. Balents, Y. Yu, G. Chen, Weyl magnons in breathing pyrochlore antiferromagnets, Nat. Commun. **7**, 12691 (2016).
- [29] M. Ezawa Higher-Order Topological Insulators and Semimetals on the Breathing Kagome and Pyrochlore Lattices, Phys. Rev. Lett. **120**, 026801 (2018).
- [30] K. Kimura, S. Nakatsuji, and T. Kimura, Experimental realization of a quantum breathing pyrochlore antiferromagnet, Phys. Rev. B **90**, 060414(R) (2014).
- [31] T. Haku, M. Soda, M. Sera, K. Kimura, S. Itoh, T. Yokoo, and T. Masuda, Crystal Field Excitations in the Breathing Pyrochlore Antiferromagnet $\text{Ba}_3\text{Yb}_2\text{Zn}_5\text{O}_{11}$, J. Phys. Soc. Jpn. **85**, 034721 (2016).
- [32] J. G. Rau, L. S. Wu, A. F. May, L. Poudel, B. Winn, V. O. Garlea, A. Huq, P. Whitfield, A. E. Taylor, M. D. Lumsden, M. J. P. Gingras, and A. D. Christianson, Anisotropic Exchange within Decoupled Tetrahedra in the Quantum Breathing Pyrochlore, $\text{Ba}_3\text{Yb}_2\text{Zn}_5\text{O}_{11}$, Phys. Rev. Lett. **116**, 257204 (2016).
- [33] G. Pokharel, A. F. May, D. S. Parker, S. Calder, G. Ehlers, A. Huq, S. A. J. Kimber, H. S. Arachchige, L. Poudel, M. A. McGuire, D. Mandrus, and A. D. Christianson, Negative thermal expansion and magnetoelastic coupling in the breathing pyrochlore lattice material $\text{LiGaCr}_4\text{S}_8$, Phys. Rev. B **97**, 134117 (2018).
- [34] Y. Okamoto, M. Mori, N. Katayama, A. Miyake, M. Tokunaga, A. Matsuo, K. Kindo, and K. Takenaka, Magnetic and Structural Properties of A-Site Ordered Chromium Spinel Sulfides: Alternating Antiferromagnetic and Ferromagnetic Interactions in the Breathing Pyrochlore Lattice, J. Phys. Soc. Jpn. **87**, 034709 (2018).
- [35] H. M. Palmer and C. Greaves, Structural, magnetic and electronic properties of $\text{Fe}_{0.5}\text{Cu}_{0.5}\text{Cr}_2\text{S}_4$, J. Mater. Chem. **9**, 637 (1999).
- [36] R. Saha, R. Dhanya, C. Bellin, K. Béneut, A. Bhattacharyya, A. Shukla, C. Narayana, E. Suard, J. Rodriguez-Carvajal, A. Sundaresan, Magnetostructural coupling and magnetodielectric effects in the A-site cation-ordered spinel $\text{LiFeCr}_4\text{O}_8$, Phys. Rev. B **96**, 214439 (2017).

- [37] K. Koepnik and H. Eschrig, Full-potential nonorthogonal local-orbital minimum-basis band-structure scheme, *Phys. Rev. B* **59**, 1743 (1999); <http://www.FPLO.de>
- [38] J. P. Perdew, K. Burke and M. Ernzerhof, Generalized Gradient Approximation Made Simple, *Phys. Rev. Lett.* **77**, 3865 (1996).
- [39] A. I. Liechtenstein, V. I. Anisimov, and J. Zaanen, Density-functional theory and strong interactions: Orbital ordering in Mott-Hubbard insulators, *Phys. Rev. B* **52**, R5467(R) (1995).
- [40] T. Mizokawa, A. Fujimori, Electronic structure and orbital ordering in perovskite-type 3d transition-metal oxides studied by Hartree-Fock band-structure calculations, *Phys. Rev. B* **54**, 5368 (1996).
- [41] H. O. Jeschke, I. Opahle, H. Kandpal, R. Valentí, H. Das, T. Saha-Dasgupta, O. Janson, H. Rosner, A. Brühl, B. Wolf, M. Lang, J. Richter, S. Hu, X. Wang, R. Peters, T. Pruschke, and A. Honecker, Multi-step approach to microscopic models for frustrated quantum magnets: The case of the natural mineral azurite, *Phys. Rev. Lett.* **106**, 217201 (2011).
- [42] Y. Iqbal, H. O. Jeschke, J. Reuter, R. Valentí, I. I. Mazin, M. Greiter, and R. Thomale, Paramagnetism in the kagome compounds $(\text{Zn,Mg,Cd})\text{Cu}_3(\text{OH})_6\text{Cl}_2$, *Phys. Rev. B* **92**, 220404(R) (2015).
- [43] D. Guterding, R. Valentí, H. O. Jeschke, Reduction of magnetic interlayer coupling in barlowite through isoelectronic substitution, *Phys. Rev. B* **94**, 125136 (2016).
- [44] Y. Iqbal, T. Müller, H. O. Jeschke, R. Thomale, and J. Reuther, Stability of the spiral spin liquid in MnSc_2S_4 , *Phys. Rev. B* **98**, 064427 (2018).
- [45] It is known that the paramagnetic Curie law in pyrochlores may only be reached at rather high temperatures, leading to possible inaccuracies in experimentally determined Curie-Weiss temperatures [71]. In the case of the breathing pyrochlores, the Curie-Weiss fits were done in a 200 K to 350 K range for $\text{LiInCr}_4\text{O}_8$ and $\text{LiGaCr}_4\text{O}_8$ [16], in a 200 K to 300 K range for $\text{LiInCr}_4\text{S}_8$, $\text{LiGaCr}_4\text{S}_8$ and $\text{CuInCr}_4\text{S}_8$ [34] and using temperatures up to 380 K for $\text{CuInCr}_4\text{Se}_8$ [9]. Note that the conclusions of this work will not change even if a 10% or 20% underestimation of the Curie-Weiss temperatures would force us to revise down the U values at which we read off the relevant model Hamiltonians in Figure 2. For the oxides, the Hamiltonian will remain in the same limit even if U is lowered substantially. The same is true for the sulfides because the FM coupling of the large tetrahedron does not depend much on U .
- [46] J. Reuther and P. Wölfle, J_1 - J_2 frustrated two-dimensional Heisenberg model: Random phase approximation and functional renormalization group, *Phys. Rev. B* **81**, 144410 (2010).
- [47] J. Reuther, P. Wölfle, R. Darradi, W. Brenig, M. Arlego and J. Richter, Quantum phases of the planar antiferromagnetic J_1 - J_2 - J_3 Heisenberg model, *Phys. Rev. B* **83**, 064416 (2011).
- [48] J. Reuther, R. Thomale, Functional renormalization group for the anisotropic triangular antiferromagnet, *Phys. Rev. B* **83**, 024402 (2011).
- [49] J. Reuther, D. A. Abanin and R. Thomale, Magnetic order and paramagnetic phases in the quantum J_1 - J_2 - J_3 honeycomb model, *Phys. Rev. B* **84**, 014417 (2011).
- [50] W. Metzner, M. Salmhofer, C. Honerkamp, V. Meden and K. Schönhammer, Functional renormalization group approach to correlated fermion systems, *Rev. Mod. Phys.* **84**, 299 (2012).
- [51] C. Platt, W. Hanke and R. Thomale, Functional renormalization group for multi-orbital Fermi surface instabilities, *Adv. Phys.* **62**, 453 (2013).
- [52] M. L. Baez and J. Reuther, Numerical treatment of spin systems with unrestricted spin length S : A functional renormalization group study, *Phys. Rev. B* **96**, 045144 (2017).
- [53] F. L. Buessen, D. Roscher, S. Diehl, and S. Trebst, Functional Renormalization Group Approach to $SU(N)$ Heisenberg Models: Real-Space Renormalization Group at Arbitrary N , *Phys. Rev. B* **97**, 064415 (2018).
- [54] M. F. Lapa and C. L. Henley, Ground States of the Classical Antiferromagnet on the Pyrochlore Lattice, arXiv:1210.6810.
- [55] Y. Iqbal, T. Müller, K. Riedl, J. Reuther, S. Rachel, R. Valentí, M. J. P. Gingras, R. Thomale, H. O. Jeschke, Signatures of a gearwheel quantum spin liquid in a spin- $1/2$ pyrochlore molybdate Heisenberg antiferromagnet, *Phys. Rev. Mater.* **1**, 071201(R) (2017).
- [56] The $T = 20$ K internal coordinates of $\text{LiInCr}_4\text{O}_8$ were privately communicated by Goran Nilson.
- [57] P. H. Conlon and J. T. Chalker, Absent pinch points and emergent clusters: Further neighbor interactions in the pyrochlore Heisenberg antiferromagnet, *Phys. Rev. B* **81**, 224413 (2010).
- [58] G.-W. Chern, R. Moessner, O. Tchernyshyov, Partial order from disorder in a classical pyrochlore antiferromagnet, *Phys. Rev. B* **78**, 144418 (2008).
- [59] R. Moessner and J. T. Chalker, Properties of a Classical Spin Liquid: The Heisenberg Pyrochlore Antiferromagnet, *Phys. Rev. Lett.* **80**, 2929 (1998).
- [60] M. Rück and J. Reuther, Effects of two-loop contributions in the pseudofermion functional renormalization group method for quantum spin systems, *Phys. Rev. B* **97**, 144404 (2018).
- [61] P. J. Brown, A. G. Fox, E. N. Maslen, M. A. O'Keefe, and B. T. M. Willis, in *International Tables for Crystallography Volume C: Mathematical, Physical and Chemical Tables*, edited by E. Prince (Springer Netherlands, Dordrecht, 2004), pp. 391399.
- [62] Private communications with Jason Gardner, Yoshihiko Okamoto and Zenji Hiroi.
- [63] C. L. Henley, Ordering by disorder: Groundstate selection in fcc vector antiferromagnets, *J. Appl. Phys.* **61**, 3962 (1987).
- [64] M. V. Gvozdkova and M. E. Zhitomirsky, A Monte Carlo study of the first-order transition in a Heisenberg FCC antiferromagnet, *JETP Letters* **81**, 236 (2005).
- [65] Y. V. Tymoshenko, Y. A. Onykienko, T. Müller, R. Thomale, S. Rachel, A. S. Cameron, P. Y. Portnichenko, D. V. Efremov, V. Tsurkan, D. L. Abernathy, J. Ollivier, A. Schneidewind, A. Piovano, V. Felea, A. Loidl, and D. S. Inosov, Pseudo-Goldstone Magnons in the Frustrated $S = 3/2$ Heisenberg Helimagnet ZnCr_2Se_4 with a Pyrochlore Magnetic Sublattice, *Phys. Rev. X* **7**, 041049 (2017).
- [66] D. Bergman, J. Alicea, E. Gull, S. Trebst, L. Balents, Order by disorder and spiral spin liquid in frustrated diamond lattice antiferromagnets, *Nat. Phys.* **3**, 487 (2007).
- [67] S. Gao, O. Zaharko, V. Tsurkan, Y. Su, J. S. White, G. S. Tucker, B. Roessli, F. Bourdarot, R. Sibille, D. Chernyshov, T. Fennell, A. Loidl, Alois, C. Rüegg, Spiral

- spin-liquid and the emergence of a vortex-like state in MnSc_2S_4 , *Nat. Phys.* **13**, 157 (2016).
- [68] J. M. Luttinger and L. Tisza, Theory of Dipole Interaction in Crystals, *Phys. Rev.* **70**, 954 (1946).
- [69] T. A. Kaplan and N Menyuk, Spin ordering in three-dimensional crystals with strong competing exchange interactions, *Phil. Mag.* **87**, 3711 (2007).
- [70] V. F. Sears, Neutron scattering lengths and cross sections, *Neutron News* **3**, 26 (1992).
- [71] L. D. C. Jaubert, M. J. Harris, T. Fennell, R. G. Melko, S. T. Bramwell, P. C. W. Holdsworth, Topological-Sector Fluctuations and Curie-Law Crossover in Spin Ice, *Phys. Rev. X* **3**, 011014 (2013).